Crystal Cell Solid-State Batteries: Testing and Variations

THESIS

Presented to the Faculty of the Department of Physics and Astronomy
in Partial Fulfillment of the Major Requirements
for the Degree of

BACHELOR OF SCIENCE IN
PHYSICS

Drew Bray

May 2024

Crystal Cell Solid-State Batteries: Testing and Variations

Drew Bray

Signature of Author:

_____

Department of Physics and Astronomy
May 2024

Certified by:

_____

Dr. Nat Smith
Professor of Physics & Astronomy
Thesis Supervisor

Accepted by:

_____

Dr. Ronald Henderson
Professor of Physics & Astronomy

ABSTRACT

This thesis delves into the electrical potentials of solid-state crystal cell batteries through systematic exploration of electrochemical designs and construction parameters. Methodology involved designing and building batteries for comprehensive testing. The study assessed the impact of substrate doping, copper cathode annealing methods, magnesium anode diameter variations, and cell mass analysis on electrical performance. Results showed significant electrochemical variations corresponding to parameter changes. Substrate doping improved ion conductivity and battery longevity. Annealing methods were shown to influence electrical properties. Varying anode diameters affected initial energy output. Cell mass analysis hinted at correlations between dopant characteristics and performance metrics. These findings offer insights for optimizing crystal cell battery design and construction, potentially advancing battery technology.

TABLE OF CONTENTS

LIST OF FIGURES

LIST OF TABLES

I. INTRODUCTION

Crystal cell solid-state batteries, commonly referred to as simply solid-state batteries, are a relatively new and emerging technology in the field of energy storage. Solid-state batteries represent a substantial improvement over traditional lithium-ion batteries including possible higher energy density, enhanced safety, and potentially a longer lifespan. The largest noticeable difference between traditional batteries and crystal cell solid-state devices can be found in the name. The phrase "crystal cell" is in reference to the unique structure of the battery's electrolyte, commonly referred to as substrate. This distinguishing feature of crystal cell batteries is in opposition to the commonly found liquid or gel electrolytes used in typical lithium-ion batteries. This substrate can typically be observed as a crystalline or glass-like material that permits free movement of ions, contained in the substrate, between the battery's anode and cathode. These crystal cell electrolytes provide a “solid-state” physical barrier between these positive and negative terminals resulting in batteries that are more resistant to overheating and are far less likely to catch on fire. Furthermore, solid-state batteries generally have a higher energy density compared to typical lithium-ion batteries. This means that solid-state batteries can generally store more energy in comparable volume, potentially leading to a longer cell life and has the possibility to be a more powerful battery. This larger energy density is particularly essential for higher computing power that is becoming more prevalent in portable electronic devices. The longer life span observed by the cell is credited to the solid-state substrate being less prone to degradation. However, crystal cell solid-state batteries face some technical challenges that still need to be resolved before they can be produced on a large scale. Currently, manufacturing crystal cell batteries has proven to be

more complex and costly compared to traditional lithium-ion batteries. Additionally, there are issues related to achieving a faster transfer of electrons in the solid-state substrate resulting in a slower discharging speed. This is where my research, under the tutelage of Dr. Smith, begins to take root. I hope the steps I have taken, and explained below, will aid in the understanding of solid-state batteries, and hasten our ability to develop a crystal cell battery ready for full production.

$$Mg \longrightarrow Mg^{+2} + 2e^- \qquad E° = 2.37V$$

$$Cu^{+2} + 2e^- \longrightarrow Cu \qquad E° = 0.34V$$

$$Mg + Cu^{+2} \longrightarrow Mg^{+2} + Cu \qquad E° = 2.71V$$

$\therefore$ The emf of cell is given by NERNST equation:

$$E_{cell} = E^{\circ}_{cell} - \frac{0.0591}{2} \log \frac{[Mg^{+2}]}{[Cu^{+2}]}$$

$$= 2.71 - \frac{0.0591}{2} \log \frac{[Mg^{+2}]}{[Cu^{+2}]}$$

Figure 1:Above shows the basic mathematical approach to understanding the electrochemical forces that all the batteries constructed during this project take advantage of to generate a portable power source. Source: (Byju's, 2023).

In general, most batteries, or cells, can be understood as electrochemical storage devices that are designed in a multitude of ways to retain and release electrical energy by

allowing electrons to pass between desired points. The main components of a general battery include the anode, cathode, and some type of electrolyte. The anode serves as a key element for controlling the flow of electrons. Within a battery this is the location where oxidation occurs, or otherwise, where electrons are lost from a material during some chemical reaction. Thus, the result of oxidation becomes the point from which electrons flow out of the battery or cell. Conversely, the cathode is where reduction takes place. Reduction is the process that can best be understood as the resulting gain of electrons during a given electrochemical exchange. The electrolyte is a material that mediates the flow of electrons between the anode and cathode. This mediation is key in maintaining the charge stability during a given electrochemical reaction.

Before explaining my research goals, it is important to understand the basis of the type of electrical cell I will be constructing and testing. For batteries electric potential between two metals, such as copper and magnesium, can best be understood by evaluating their base electrical properties. Electric potential, more commonly called voltage, is simply the potential energy per unit of charge at any given point. Usually this can be thought of as the potential difference between any two points. This potential is what tells us how much energy is required to move charged particles, electrons or positive 'holes', from one place to another. The standard reduction potential of Mg is -2.37V and Cu is +0.34V, so if we want to know the maximum potential difference we must subtract the Mg potential from the Cu potential, giving us +2.71V. This found maximum potential is the absolute most amount of induced voltage that these two specific metals can generate. This might not sound like a lot but, the most commonly used battery voltage for most small objects is

1.5V. This means that copper and magnesium could produce an even more powerful battery than the well-known AA or AAA variants that are used worldwide. It is my intent to construct and test crystal cell batteries with various differences to observe and compare total voltage output, longevity, and total full cell amperage. I want not only to compare these crystal cells against one another but, verse more commonly used mainstream batteries.

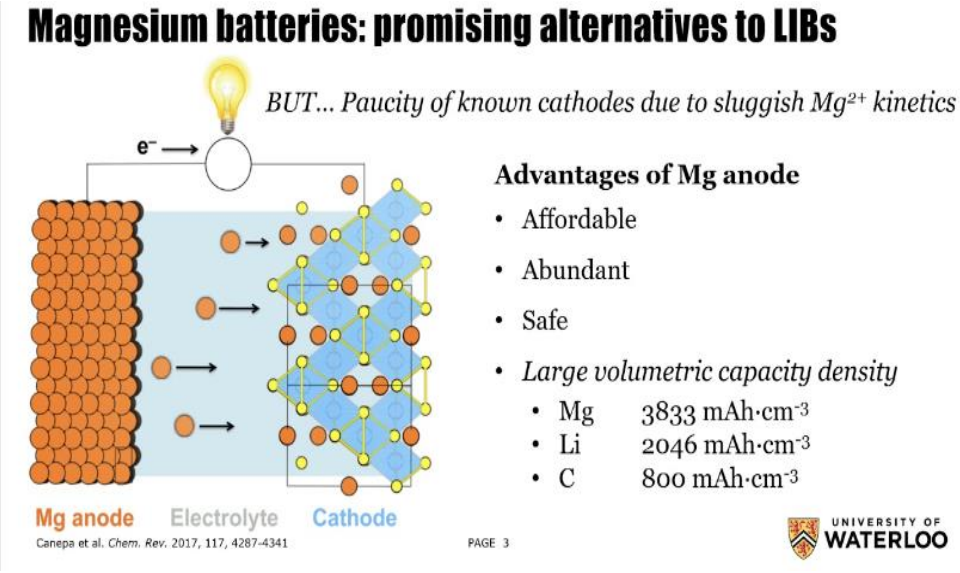

Figure 2: Above shows yet another reason for investigation into the Mg-Cu cells. Source: (Blanc, 2020)

II. Methodology

A. Fabrication of Tested Cells

The main components of the crystal cell batteries that were constructed for this research were comprised of a copper cathode, a magnesium anode, and the salt substrate that bridges the path between the two. The copper cathode was made from 2.53 cm diameter copper piping and also acted as the battery casing. The magnesium anode used was chosen to be a solid rod that resides in the center of the copper cathode but is not allowed to directly touch. The anode diameter is particularly interesting in this experiment due to this component being largely responsible for altering the volume of allowable crystal substrate within the cell's interior. This ability to alter the inner cell was chosen as a means to alter the cells and resulted in the use of two different size diameter anodes whereby allowing a variation in the constructed cells and allowed data to be collected by observing how the differences in diameter affected the cells output. The different anode diameters used were the larger 0.95 cm diameter and the smaller 0.80cm diameter. All measurements for the cells were made using a set of electric calipers made by MITUTOYO. The substrate base for each of the crystal-cells are all comprised of the same base composition. Where all of the cells that were constructed were comprised of equal parts by mass of this substrate base that consists of, aluminum potassium sulfate dodecahydrate ($KAl(SO_4)_2 \cdot 12H_2O$), magnesium sulfate heptahydrate ($MgSO_4 \cdot 7H_2O$), potassium chloride (KCl), and sodium tetraborate ($Na_2B_4O_5(OH)_4 \cdot 8H_2O$). The four aforementioned salt compounds were melted together by different hand torches to almost 1000 °C and poured into the toroidal

cavity between the magnesium anode and copper cathode. After the crystal substrate cooled and solidified it acted as an ion bridge that connected the main components of the batteries.

The fabrication of the cells used in this experiment started by cutting the copper cathodes into equal lengths of 5.40 cm. After the cathodes were cut, I then went forward by drilling and tapping pilot holes in the top of the Magnesium rods. This alteration of the anode allowed me to insert a 6 mm x 1.25 bolt. I then used this bolt to attach a ring terminal that allowed me the ability to easily check electrical values of the battery.

Figure 3: Above shows the alteration made to the anodes as described above.

This alteration was performed using a drill press to assure that the holes were centered in each anode equally. The differing diameters used for the anodes during this experiment

were all outfitted with this same design in order to neglect any unwanted differences in observed internal resistance values.

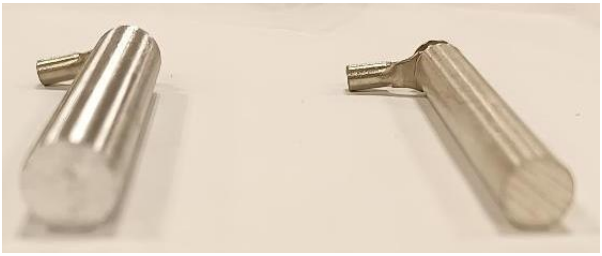

Figure 4: Showcased above are the anode variants used during testing. The anode on the right is a 99.9% pure magnesium rod that is 8mm in diameter and the rod on the left is composed of the same purity but is 9.5mm in diameter.

Next, I had to design a way that I could hold the rod in place, the center, while assuring that the rod is physically prevented from touching the cathode walls. This was achieved by using a polyurethane grommet that was drilled out to firmly hold the anode and given a lip around the circumference to assure that the grommet has adequate friction against the cathode walls and prevent the anode from moving laterally when the substrate is added.

Figure 5: Above shows the polyurethane grommets used next to the copper cathode that they were fitted into.

After the grommets were fabricated, I next utilized the drill press again to pilot the holes that were used to attach another 6 mm x 1.25 bolt, 6 mm adjoining nut, and a fork terminal fitting. The fittings that were used for the cathode were again standardized to prevent ranging results in the values observed in the experiment.

Throughout the fabrication process efforts were made to prevent unwanted variations between the cells. Specifically, special efforts were made to prevent oxidation of the anodes. In between the stages where the anodes were drilled and outfitted with the fittings, they were placed into individual airtight plastic bags. This isolation process was practiced throughout the term of the experiment.

Figure 6: Shows the test anode used to assure that the parts were fabricated correctly. Note the discoloration observed on the anodes surface. The isolation in air-tight plastic bags prevented this from occurring to the anodes that were used in this experiment.

After the aforementioned steps were taken, the cells were assembled and ready for the substrate to be added. The cells were filled with the melted substrate individually and allowed to cool before observing the completed mass of each cell and being placed in isolation again. All mass measurements taken throughout the experiment were made using a RESHY high precision lab scale.

Figure 7: Here is the final test fabrication model that was made for the crystal cells. Note that none of the items displayed above were physically used in the tested cells and were only used as proof of concept.

Figure 8: Here is the same test fabrication model but shown from a top-down view. Note, special attention was taken to prevent the bolt head from bridging the cavity between the magnesium anode and the copper cathode and causing a short in the battery.

B. The Annealing Process

The central aim of the research is geared towards evaluating and testing each battery variation that could lead to an observable difference in the battery's amp-hours, voltage difference and cell life. One such battery variation I evaluated was to anneal the copper cathode of the battery with sodium tetraborate ($Na_2B_4O_5(OH)_4 \cdot 8H_2O$). Annealing is a process whereby heating a metal and allowing the sample to be cooled in a controlled manner, the properties of a metal can be enhanced. With respect to this project the controlled cooling was done using a quench tank whereby rapidly cooling the cathode and allowing the copper atoms within the metal to be rearranged in specific crystalline patterns.

Figure 9: Above is the quench tank that was fabricated so that the cathodes could be quenched using distilled water and sodium tetraborate to create a super saturated solution.

The purpose of annealing the copper cathode was to first create copper (II) oxide, or also known as cupric oxide, which has a chemical formula of (CuO); by heating the metal to just below the melting point of copper which is approximately 1,084 °C. Copper (II) oxide is formed when elemental copper losses two of its electrons to oxygen and consequentially this bonding results in a monoclinic crystal structure. A monoclinic crystal can best be described as, a crystal system by which the structure of the crystal is comprised of three nonequal axes of different observable lengths whereby two of the crystal planes meet at an oblique angle, and the third plane of the crystal is perpendicular to the other two. Specifically, this result, and this crystal structure was one of the justifications for using copper cathodes; due to one of the general properties of monoclinic crystals being that they may offer some piezoelectric aspects and that the oblique angles in the crystal structure allow the certainty of cleavage lines that can be used for further bonding potential. These cleavage lines can be exploited during the quenching process where while the metal is being rapidly cooled, in a super saturated solution, elemental bonding can occur more heavily in the cleavage lines and drive a transformation of the metal's atomic structure.

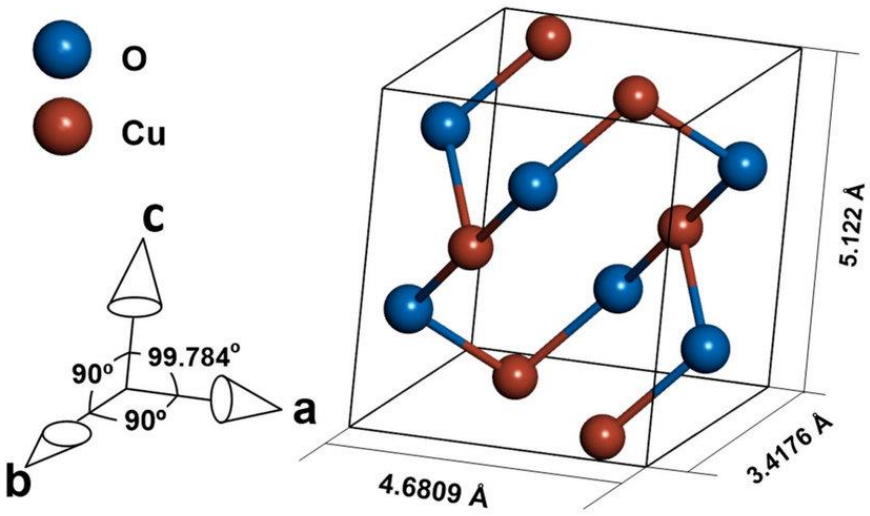

Figure 10:Above shows the crystal structure that causes the cleavage lines discussed. Source: (Researchgate, 2020).

In regard to the steps taken during this project, first I had to sand the oxidized layer of copper off the intended cathodes. Next, I had to bring the copper up to a temperature that would allow the metal to readily make new bonds, this was accomplished by heating the copper cathode, by hand using a torch, to approximately 925 °C whereby this temperature was confirmed using a handheld metallurgical IR temperature sensing gun. Next, the newly formed copper (II) oxide cathode was quickly transferred to the quench tank in a super saturated solution that consisted of 150 g of sodium tetraborate ($Na_2B_4O_5(OH)_4 \cdot 8H_2O$) that was suspended in 500 mL of distilled water.

Figure 11: From right to left, the image above first shows the cathode style that will be used for the majority of the batteries tested, the next, middle cathode, has been sanded down to allow the cathodes to be annealed, and the left most cathode shown is one that has been annealed using propane as a heating source.

These processes were completed multiple times using two different methods of heating the cathodes. The first method to heat the cathodes was by using a propane torch, which has a chemical formula, C_3H_8 however, propane gas also has the additive ethyl mercaptan for safety reasons and has the chemical formula, C_2H_6S.

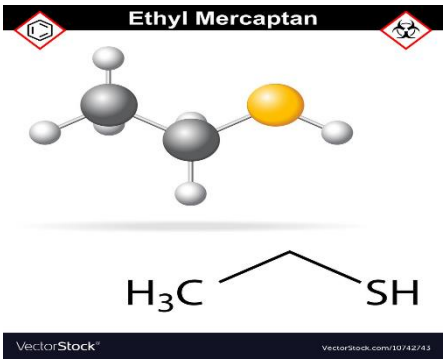

Figure 12: When sufficient energy is expended the result is the sulfur atom becomes positively or negatively charged. This is the property that would cause the formation of an unwanted bond to the cathode during the annealing process. Source: (Logos2012, 2016)

Figure 13:Above is the result of the annealed cathodes using the propane torch to heat the cathodes to 925C. This coloring was an unexpected result and I believe it is due to the additive in the propane that gives it a smell.

Figure 14: Above shows the physical difference between the cathodes that were annealed using the propane heating and the non-annealed cathodes.

Since propane gas has an additive that is introduced during the heating of the cathode the decision to use more than one method of heating the cathodes was made. The second method to heat the cathodes was using Acetylene, a hydrocarbon gas that burns cleaner and significantly hotter, with a chemical formula C_2H_2. This difference in the source of heating was the only difference made in the steps to annealing the copper cathodes. The copper cathodes heated in this manner were still quenched in the same tank, in 500 mL of distilled water, and the solution that was used still consisted of 150 g of sodium tetraborate ($Na_2B_4O_5(OH)_4 \cdot 8H_2O$).

Figure 15: Note the drastic difference of coloration between the two different heating techniques. It is also worth mentioning that the texture of the two metals is not the same and there was clearly a different reaction that occurred.

After being subjected to the annealing process, the cathode should act as a semiconductor and the base substrate was then added to the annealed cathode and installed anode. The use of semiconductors in battery technology has been gaining popularity in the industry for many reasons. Mainly, this is due to semiconductor materials such as silicon carbide, which has the chemical formula (SiC), and others like gallium nitride, which has the chemical formula (GaN), have been observed to aid in the ability for batteries to exhibit faster charging times. Additionally, semiconductor materials seem to enable cells to store higher power densities, while also preserving the observed thermal stability. Thus, the addition of semiconductor materials aids in reducing the observed time it takes for the ions to transverse throughout the battery significantly. However, this high-tech addition to the

cells I fabricated may affect the overall lifetime of the batteries. Luckily, this adverse effect should be mitigated by the extremely long lifespan observed in crystal cell batteries.

Figure 16:Above shows a cell made in a very similar manner to the cells constructed for this experiment. The cell shown has been bisected down the middle in an attempt to observe the degradation of the cell. This specific cell was used in conjunction with other crystal-cell batteries to operate a motor that started spinning in December 2011 and was observed to run for 1429 days. Source: (Lasersaber, 2015).

C. Solid-State Crystal Cell Doping

Throughout this experiment I have also varied the batteries by doping the substrate with different compounds that aim to aid in allowing the ions to flow through the crystal and hence give a larger observed current. Doping a substance is the action of intentionally introducing impurities, typically in small percentages, into the body of a substance in hopes of modifying some of its properties. In regard to electrical applications, this practice is

generally used for the creation of semiconductor materials. The process of doping a semiconductor is used to meter the materials conductivity and other various electrical actions. While performing the action of doping, different atomic elements are introduced into a crystal lattice of a material and depending on the materials crystal structure the atoms being added into the crystal lattice can have profound effects on the properties of the material. These effects are driven by how the dopant, the material being added to the base compound, affects the electron shells of the material being doped. These outer shells of electrons are called the valence electrons and if the dopant causes the material to have extra electrons that are free to become mobile, then this is typically described as n-type doping. For n-type doping, an excess of electrons in the material will often exhibit a material with higher electron conductivity properties. Conversely, if a material is dopped in such a manner that the material now has an electron deficiency due to the dopant being inserted into the crystal structure, this is called p-type doping. However, this lack of electrons also improves the materials conductivity due to this causing the passive pull of electrons into the material. This pull of electrons or observed lack of an electron in the crystal lattice is often referred to as a “hole”.

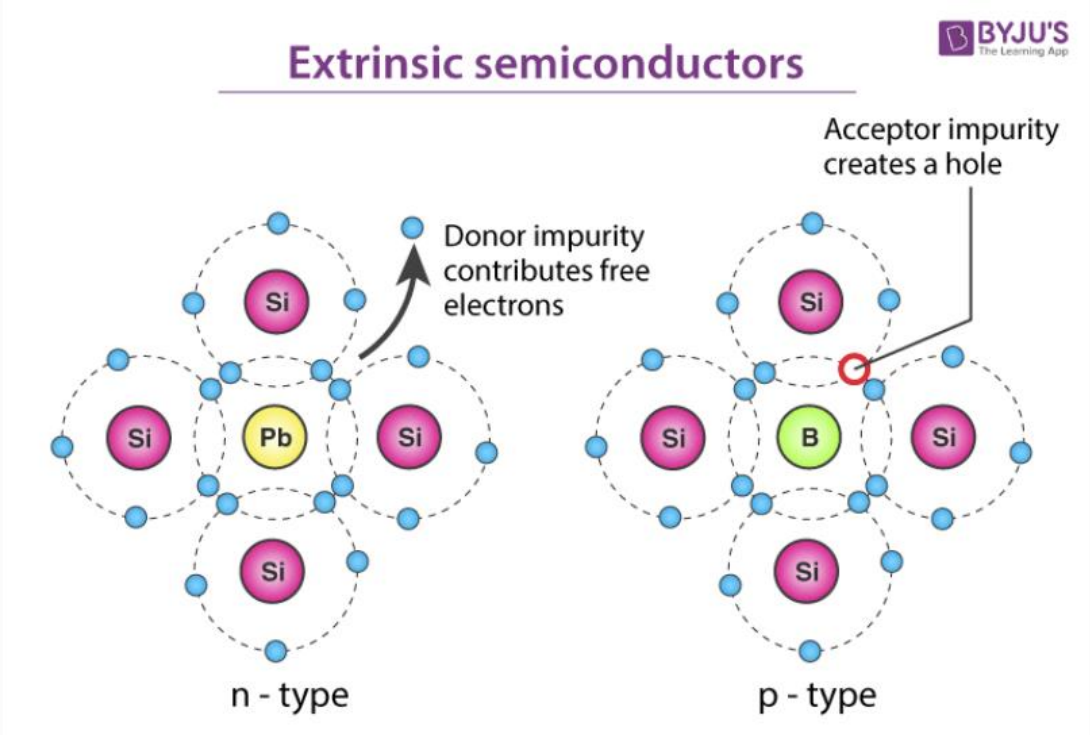

Figure 17: Above is a visual depiction showing the difference between the types of doping that can be utilized when analyzing different chemical components for the crystal substrate. Source: (Byjus, 2023).

Due to the possibility that doping the substrate could lead to improved properties of the cells I chose to dope cells during this experiment. I chose to use iron sulfide, potassium sodium tartrate tetrahydrate, and sodium carbonate for the tested dopants. In each case the dopants were added in small amounts in respect to the mass of the base substrate. These materials were always added into unaltered base substrate and mixed into the base substrate just prior to being melted together to avoid any contamination. The specific choice of dopants was due to the commonality found in other research projects.

III. Testing

After the construction of the batteries was finished, I set forth to analyze electrical properties of these cells. Shortly after allowing the crystal substrate in the cells to cool, I found the short circuit amperage, new mass measurements, and initial observed voltage for each cell. In order to test the longevity and stability of the constructed cells I have also tested the solid-state crystal cell batteries again after 110-days of time had elapsed from the time that the initial readings were taken. In this round of tests I tested the observable voltage, time that the crystal cells took to reach specific percentages of full charge after being subjected to being placed into a short circuit, each cell constructed being tested against ten differing amounts of resistance that range from 1 Ω to larger values up to 1 MΩ and observing the amperage for each cell for specific amounts of resistance. For the sake of brevity, I have also fabricated a cataloging system to quickly reference the cells in tables and graphs for the annealed cells that were constructed. The cataloging system is interpreted as follows; (diameter . heat source . annealing rounds) diameter size of anode used denoted as (B) for larger diameters or (S) for smaller diameters, heating source used for annealing denoted as (A) for acetylene or (P) for propane, and number of times the heating process was conducted on that specific cathode denoted as 1H, 2H or, 3H where the numeral here is used to index how many rounds of heating/annealing that the cell was subjected to. The scope of the results regarding longevity are ongoing, and I will continue to collect data for this parameter of this project until I find that the cells are beginning to fail.

A. Voltage Testing of Cells

Shortly after the newly constructed cells were cooled, the first testing done on the batteries was in regard to voltage. The initial readings and later base line voltages were achieved by simply using a digital multimeter set to DCV and touching the probes to the testing locations of the anode and cathode. The more comprehensive voltage testing of the batteries using varied amounts of resistance required building a simple circuit to analyze the voltage acting on a load. To obtain voltage readings from a digital multimeter connected to a battery in conjunction with a resistance, the multimeter was again set to the voltage measuring range DCV. Next, the battery was connected to the circuit with the positive terminal, or cathode, connected with alligator clamps to the positive lead of the multimeter and the negative terminal, or anode, connected to the negative lead with the same type of clamps used for the cathode. Following this, various resistors were implemented in series with the battery, by connecting the positive lead of the multimeter and cathode to one terminal of the resistor, and the negative lead junction to the point of the other terminal of the resistor. The multimeter was always given time to allow the display to read a steady constant voltage drop across the resistor and recorded. This resistance source was then changed, and the new voltage drop was then recorded, this is the same process that was carried out for each cell. Below in figure 18, the process described is demonstrated graphically.

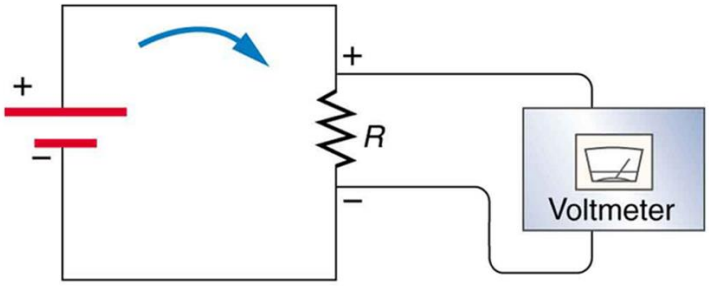

Figure 18: Graphic representation showing the basic method to testing a voltage drop across a load. Source: (BCIT Physics)

Since one of the key characteristics of solid-state crystal cell batteries is the ability to rapidly rejuvenate their observed electrical potential after a load or resistance has been removed, tests were conducted that observed the time it took to observe this voltage 'bounce back' between the variations of the constructed cells. This test was accomplished by exposing the cells to a 1Ω resistor until the voltage observed by a digital multimeter dropped to zero volts. After this short circuit occurred the resistor was removed, and the electrical potential of the tested cell was allowed to rejuvenate. To take measurements of this test the voltages were viewed by using a digital multimeter set to DCV and touching the positive probe of the multimeter to the cathode and the negative probe of the multimeter was attached to the anode. A digital stopwatch was then utilized to monitor the time intervals between the cells rising from zero volts to 50%, 80%, 90%, and 95% of the measured full steady state voltage for each constructed cell.

B. Comparison of Currents Observed in Cells

Following the initial voltage readings the next value obtained was the test for short circuit current. Typically, to assess short circuit readings with a digital multimeter with regard to a battery, first, the battery must be disconnected from any circuit or possible path that would allow the electrical potential to flow. After isolation is accomplished, the digital multimeter would be set to measure resistance, denoted by the symbol Ω. Next, the normal procedure to find short circuit current would archetypally be to connect the positive lead of the digital multimeter to the positive terminal of the battery and the negative lead of the digital multimeter to the negative terminal of the battery. This method of finding a short circuit current will result in very low observable resistance and thus, it is critical to perform this measurement with extreme care. However, this is not a possible method for solid state crystal cell batteries, due to the very large internal resistance values observed. So, the steps above were carried out with a few key differences; an oscilloscope was used to quickly capture values and the digital multimeter was not set to observe resistance but, instead to observe amperage. This method of finding a short circuit current in a battery is, in a sense, using the digital multimeter as the load for the battery and if done incorrectly can result in damage being done to the multimeter. Additionally, this method of finding short circuit current will result in a very brief time that the full short circuit current is observable and hence, it was important to perform this measurement methodology with the use of a device that can record electrical values.

The short circuit current was not the only current measurements that were taken to compare the constructed cells. Tests were also carried out in the later tests using the same resistors that were used to find voltage drops in the cells. This was accomplished by using the resistors that gave the most steady and largest voltage measurements to obtain the most consistent, yet small, amperage readings. This test was conducted by connecting the digital multimeter, the cell being tested, and various amounts of resistance all in series with one another. This can be realized by first taking the cathode terminal of the battery and connecting it to the positive lead of the digital multimeter. Next, connect the negative lead of the digital multimeter to one terminal of the resistor and similarly connect the other terminal of the resistor to the anode terminal of the crystal cell. The multimeter was always given time to allow the display to read a steady constant current flow through the circuit and recorded. This resistance source was then altered, and the new current flow through the circuit was then recorded. After all resistance values were exhausted the cells were changed and the same steps were carried out for each cell. In figure 19, the aforementioned process described is exhibited clearly.

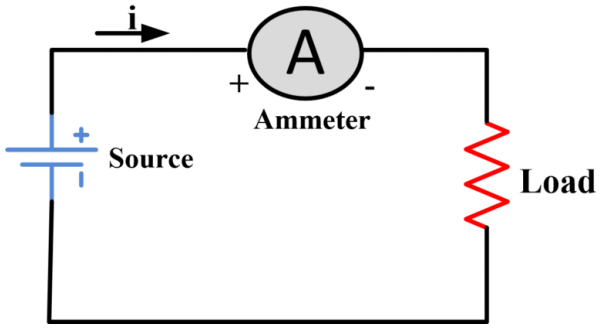

Figure 19: Graphic representation showing the basic method of testing a current flowing through a circuit. Source: (Faizan, A, 2024).

C. Variations of Cell Mass

Testing the variations in observed mass of the different crystal cell batteries that were constructed is fundamental for understanding the battery's performance. This can best be justified in this experiment since anode diameters were not consistent across all constructed cells, the typical mass of a solid-state battery with similar volume as a traditional electrolytic cell is normally larger, and the mass of a cell determines how it can be implemented in the world. Furthermore, understanding the mass flow of each cell provides insights into the battery's performance and potential future improvements. Additionally, variations in cell mass could be indicative of observed inconsistencies that could affect battery efficiency and reliability Moreover, the testing of the mass of different solid-state crystal cell batteries and their components will allow further research that will provide the opportunity to monitor changes of certain properties over time, thus providing

valuable data on the mechanisms driving solid-state crystal cell battery degradation. This data can be cataloged by periodically measuring the major component masses for each constructed cell and by tracking the degradation trends strategies can be designed to mitigate unwanted mass loss in specific crystal cell components. Ultimately, understanding the mass of the crystal cell battery components and examining the expected variations over time is essential for advancing battery technology and the overall reliability of crystal cell batteries.

The testing process of the mass for the different crystal cell batteries began by carefully assembling all battery components in a methodical and standardized process as possible. Once the cells assembly process was designed, I used a precise scale to measure the mass of each type of anode diameter used and the cathode/ housing system components separately. After I found the values associated with these major components, I worked diligently to affirm that the mass for each constructed cell was held to these benchmarks. Moving forward, after the cells were heated and the substrate was added into each cell cavity, the new total mass was recorded, and this was accomplished by yet again using a precise scale to measure the mass. Here is where the cells chemistry began to interject unwanted results in the observed mass of each cell. Ideally the mass of each solid-state battery should be as similar as possible to achieve fair and uniform comparisons. However, in the heating process the substrate began to demonstrate effervescence and had to be slowly heated while being vibrated to prevent empty cavities from forming in the crystal as it cooled. This behavior is due to the reactions between the salts being mixed together and propagated in a sporadic manner.

Due to this critical step being the main source of inconsistencies to the cell mass, analyzation into these variations caused by the chemical reactions will identify areas for optimization and develop strategies to enhance battery performance. Specifically, to this end, I implemented analyzation by observing the cells mean, median, and mode of the masses in aim to gather data that will help to improve or prevent anode/cathode deposition techniques through the action of optimizing crystal cell formulations.

In the results section the component mass of each cell is given and what percentage of the total mass that each component accounts for of that specific cell. These values are the observed total masses that were recorded par the step allocated above. These individual masses provide insight into each independent cell. However, in the attempt to provide further data, the solid-state cells were then compared as a group where the mean, median, and mode of the masses are also analyzed. The mean mass is often referred to as the average and was calculated by summing up all the masses in this set of data and then dividing by the total number of masses observed. The median mass is best understood as the middle value of the crystal cell data set masses. This is found when the masses are arranged in an incremental or decremental sequence. Thus, it follows, if there is an odd number of masses, like the data set for this experiment, the median is the middle value. Unlike the mean, the median is not influenced by extreme values or outliers in the recorded cell mass data. Lastly, mode is the measurement that represents the mass value in the data that appears most commonly. In conclusion, the mean calculates the average value of the masses, the median identifies the middle mass value, and the mode focuses on the frequency of

occurrence of the most commonly recorded value. All three of these statistical methods were used to look for closely at not just the mass values of the collection of cells but also at the density and molar mass of the dopants used in the doped cells.

IV. Results

The experiment yielded predominantly conclusive and enlightening results, shedding light on various aspects of crystal cell batteries. Nonetheless, amidst these findings, numerous inquiries persist regarding the nature of these batteries and the insights gleaned from the collected data. Presented here are the sets of data originating not only from the initial creation of the solid-state crystal cells but also from the analysis conducted after allowing the solid-state cells to undergo a dormancy period of 110 days. Throughout this dormancy period, the cells were meticulously stored in airtight plastic bags, safeguarded from exposure to temperature extremes or direct sunlight, ensuring the preservation of their integrity. It's noteworthy that all subsequent data plots were meticulously generated and coded using Python, ensuring accuracy and consistency in the analysis.

It is paramount to express that the findings of this experiment only encapsulate a small fraction of the anticipated longevity of the tested crystal cells. Furthermore, the identification of several anomalies associated with dopant materials has been particularly detailed in the results presented below. In the pursuit of advancing the understanding

regarding the electrochemical capabilities locked inside these cells, it is imperative to persist in the continuation of exploration regarding the anomalous parameters discovered henceforth. My commitment to gathering further data will endure until signs of cell degradation become evident. What ensues is the dataset carefully collected to fulfill the requirement for a conclusive endpoint to this phase of the research pertaining to this project.

A. Voltage Potentials Exhibited by Crystal Cells

The tabulated data presented below in Table 1 represents the initial voltage values observed on the day the cells were constructed. These voltage measurements are anticipated to reflect the highest values observed throughout the entirety of the experiment due to the ions in the salt crystals being still warmer than room temperature and recently bonded. At this step in the project, the vast majority of the data collected exhibits voltage potentials comparable to those commonly associated with standard cells such as AA or AAA batteries. Figure 21 provides a visual representation, illustrating that the highest electrical potential was generated during this set of tests was produced by the S.A.2H cell, while the lowest value was observed in the solid-state cell doped with $FeSO_4$. The remaining cells generally exhibit similar initial voltage levels and thus provide no further insight.

Table 1: Initial Voltage Values

Cell Tested	S.A.2H	B.A.2H	B.P.1H	B.P.2H	B.P.3H	Control	B. $FeSO_4$	B. $KNaC_4H_4O_6$	B.NaCO
Initial Voltage	1.65V	1.50V	1.53V	1.46V	1.52V	1.56V	1.20V	1.44V	1.44V

Table 1: Shows the initial voltage values. Note that the voltage values observed here should be the largest observed throughout the experiment.

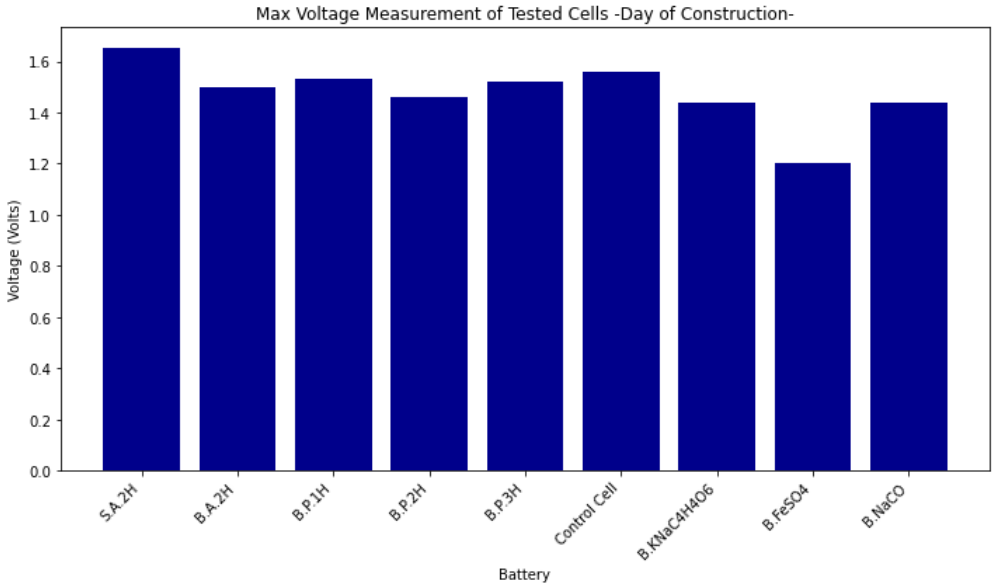

Figure 20: Graphical representation of the data tabulated in Table 1.

The results obtained from the data tabulated for the solid-state crystal cells after being isolated for 110-days yielded interesting variances. Firstly, it is noteworthy that the initial voltage reading for the $FeSO_4$ cell was lower than the value observed 110-days later. Thus, ranking it among the highest observed voltage values measured from the cells at this point in the experiment. Conversely, another notable observation is the significant decrease in voltage potential observed in the B.A.2H cell, which has dropped to a staggering 57% of

its initial voltage potential. Interestingly, apart from the $FeSO_4$ cell, all other cell potentials have decreased, which aligns with expectations. However, it's also pertinent to highlight the observation that the voltage potentials witnessed by the B.NaCO cell, when compared against each other cell, exhibited a smaller deviation in electric potential than any other crystal cell tested in this study. This nuanced variation in voltage potential suggests the possibility of unique behavior being made evident by the B.NaCO and $FeSO_4$ cells.

Table 2: Voltage Values 110-Days Later

Cell Tested	S.A.2H	B.A.2H	B.P.1H	B.P.2H	B.P.3H	Control	$FeSO_4$	B. $KNaC_4H_4O_6$	B. NaCO
Voltage	1.19	0.86	1.20	1.25	1.24	1.26	1.32	1.15	1.33

Table 2: Shows the voltage values observed after the cells sat for 110-days.

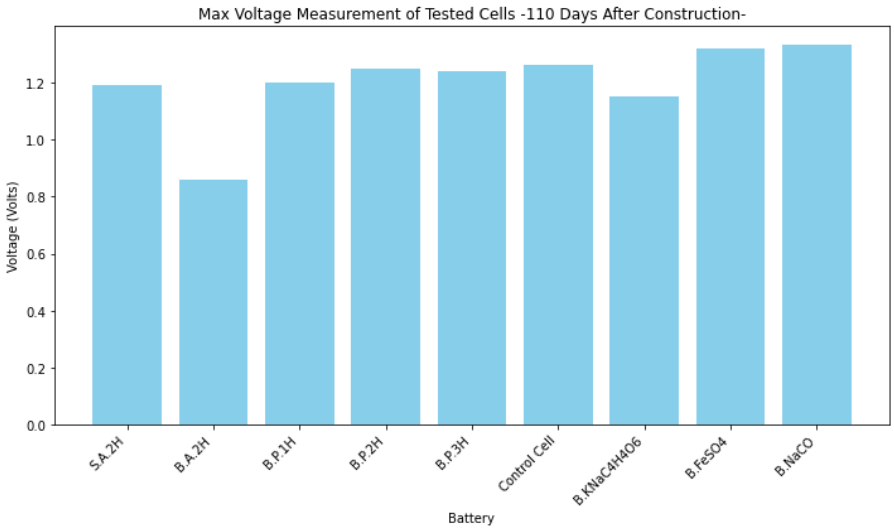

Figure 21: Graphical representation of data tabulated in Table 2. Note $FeSO_4$ cell has actually increased.

The minute voltage delta observed in the B.NaCO cell is distinctly visible in Figure 24, along with the discernible rise in electrical potential exhibited by the $FeSO_4$ cell. Furthermore, a noteworthy observation also emerged in the observance of the B.P.1H, B.P.2H, B.P.3H, and the control cells all maintaing relatively close voltage measurements across both datasets. This trend suggests that the varied annealing processes conducted on the solid-state cells cathode's are beginning to manifest distinct electrical properties. This implication could also suggest flaws of the annealing techniques used and subsequently generating negative impacts on specific crystal cell's performance.

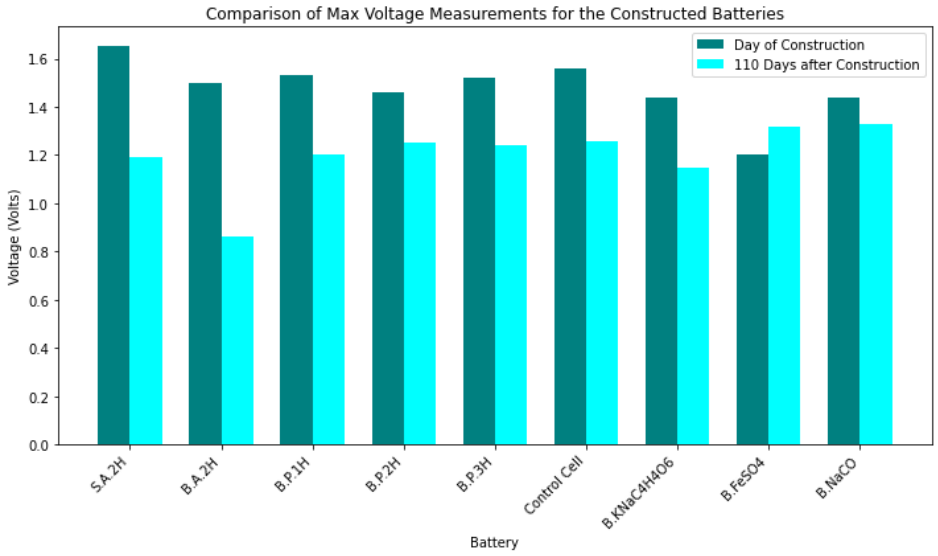

Figure 22: Graphical representation of data being compared for the tabulation of Table 1 and Table 2. Here it is easy to see the voltage increase found in the $FeSO_4$cell has actually increased.

The data presented in Table 3 and additionally in Table 4, along with the numerous subsequent plots, pertain to the voltage values obtained during testing of the crystal cells in a series circuit with varying levels of resistance. The resistor values utilized in this comprehensive test span a wide range, from as small as 1 Ω to a maximum of 1 MΩ. Within this spectrum of resistance values, it's readily apparent how the lower limits of resistance result in a short circuit scenario. However, the interpretation of the upper limit of resistance, particularly the 1 MΩ resistor's ability to effectively reduce the measured voltage of the cells to near zero, may not be immediately intuitive. To comprehend this intriguing outcome, it's imperative to delve into the underlying mathematical expression:

$$(\lim_{R\to\infty})(I) = Voltage = 0$$

The expression above reveals that as the resistance approaches infinity, the circuit can be conceptualized as an open circuit, effectively disconnected. Consequently, for exceedingly large resistance values, the electric potential experiences a gradual decline whereby, ultimately approaching zero. This mathematical principle reinforces the observed results tabulated below, where the 1 MΩ resistor induces a significant drop in observable voltage.

Table 3: S.A.2H Voltage Values for Resistance Tests

Cell Tested	S.A.2H									
Resistance	1 Ω	11 Ω	100 Ω	105 Ω	68 KΩ	100 KΩ	219 KΩ	470 KΩ	690 KΩ	1M Ω
Voltage	0.00V	0.02V	0.02V	0.03V	1.08V	1.13V	1.17V	1.16V	1.11V	0.14V

Table 3: Shows the voltage values found for each subsequent test of varied resistance observed after the cells sat for 110-days for the S.A.2H cell.

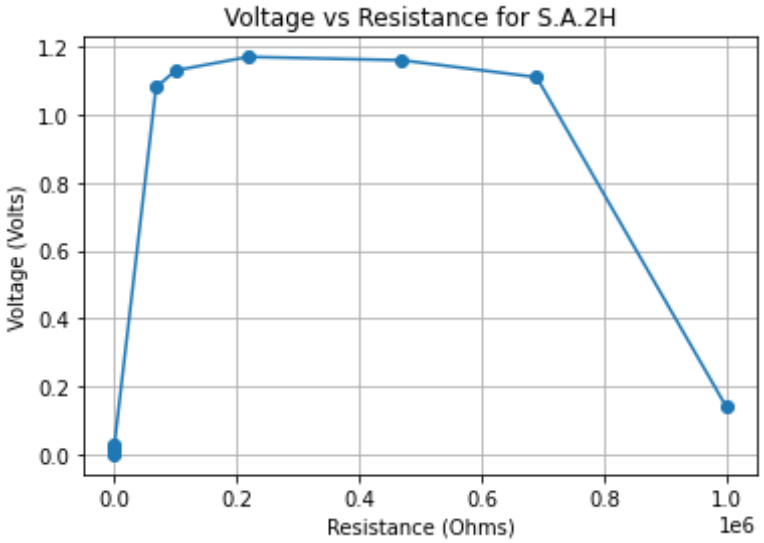

Figure 23: Data set plot for the S.A.2H cell showing observed voltage at varying resistance.

Table 4: B.A.2H Voltage Values for Resistance Tests

Cell Tested	B.A.2H									
Resistance	1 Ω	11 Ω	100 Ω	105 Ω	68 KΩ	100 KΩ	219 KΩ	470 KΩ	690 KΩ	1 MΩ
Voltage	0.00V	0.01V	0.04V	0.04V	0.69V	0.74V	0.79V	0.81V	0.83V	0.18V

Table 4: Shows the voltage values found for each subsequent test of varied resistance observed after the cells sat for 110-days for the B.A.2H cell.

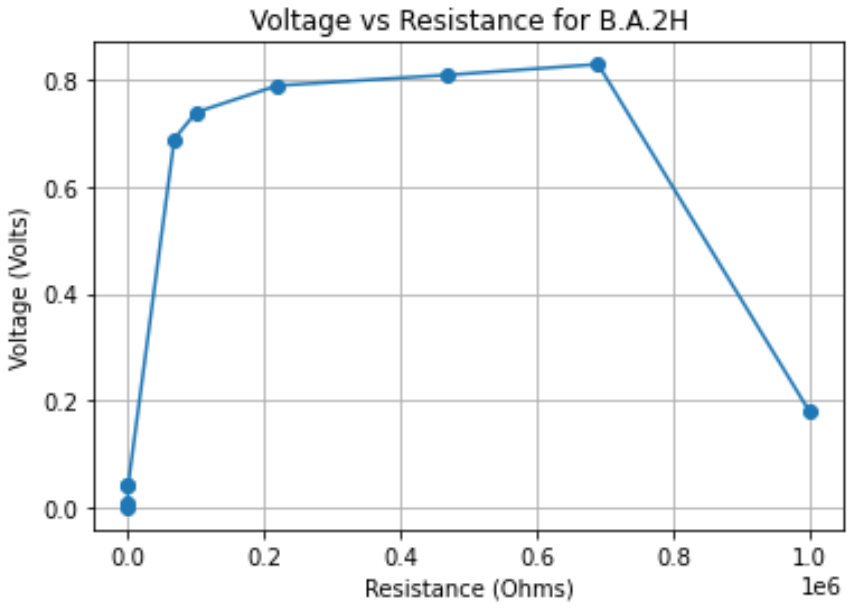

Figure 24: Data set plot for the B.A.2H cell showing voltage values observed at differing resistance values.

Table 5: B.P.1H Voltage Values for Resistance Tests

Cell Tested	B.P.1H									
Resistance	1 Ω	11 Ω	100 Ω	105 Ω	68 KΩ	100 KΩ	219 KΩ	470 KΩ	690 KΩ	1 MΩ
Voltage	0.00V	0.01V	0.05V	0.05V	1.08V	1.11V	1.14V	1.05V	1.03V	0.21V

Table 5: Shows the voltage values found for each subsequent test of varied resistance observed after the cells sat for 110 days for the B.P.2H cell.

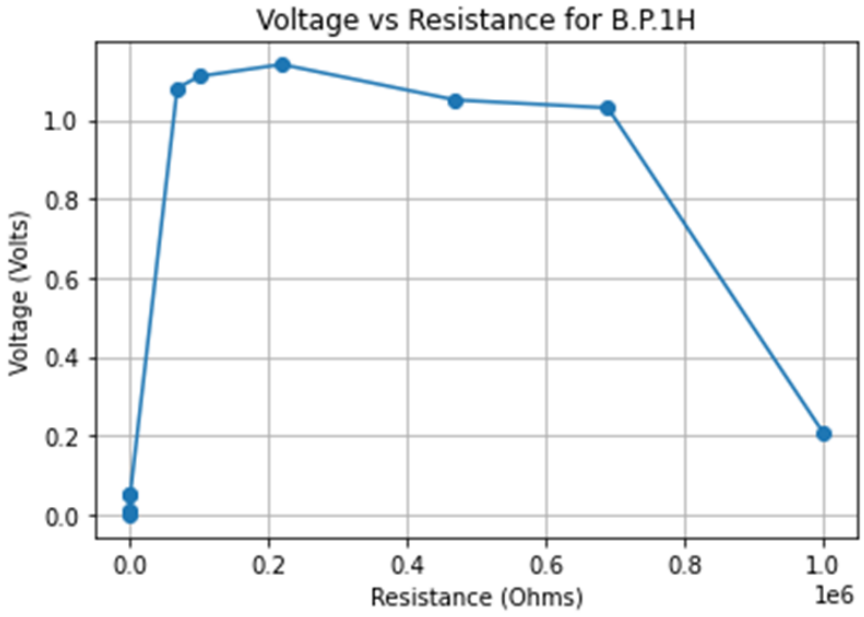

Figure 25: Data set plot for the B.P.1H cell showing voltage values observed at differing resistance values.

Table 6: B.P.2H Voltage Values for Resistance Tests

Cell Tested	B.P.2H									
Resistance	1 Ω	11 Ω	100 Ω	105 Ω	68 KΩ	100 KΩ	219 KΩ	470 KΩ	690 KΩ	1 MΩ
Voltage	0.00V	0.00V	0.05V	0.05V	1.06V	1.09V	1.12V	1.13V	1.14V	0.25V

Table 6: Shows the voltage values found for each subsequent test of varied resistance observed after the cells sat for 110-days for the B.P.2H cell.

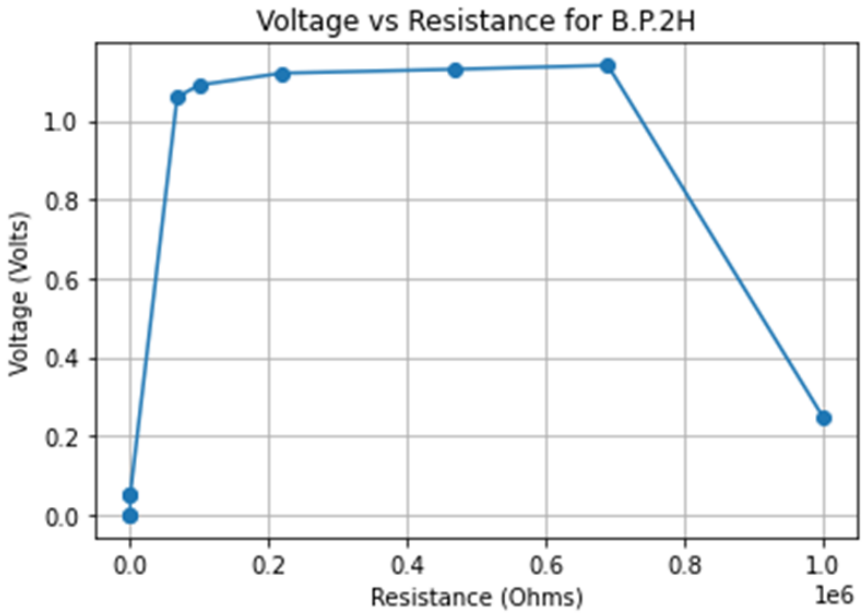

Figure 26: Data set plot for the B.P.1H cell showing voltage values observed at differing resistance values.

Table 7: B.P.3H Voltage Values for Resistance Tests

Cell Tested	B.P.3H									
Resistance	1 Ω	11 Ω	100 Ω	105 Ω	68 KΩ	100 KΩ	219 KΩ	470 KΩ	690 KΩ	1 MΩ
Voltage	0.00V	0.00V	0.04V	0.04V	1.08V	1.11V	1.15V	1.17V	1.19V	0.20V

Table 7: Shows the voltage values found for each subsequent test of varied resistance observed after the cells sat for 110-days for the B.P.3H cell.

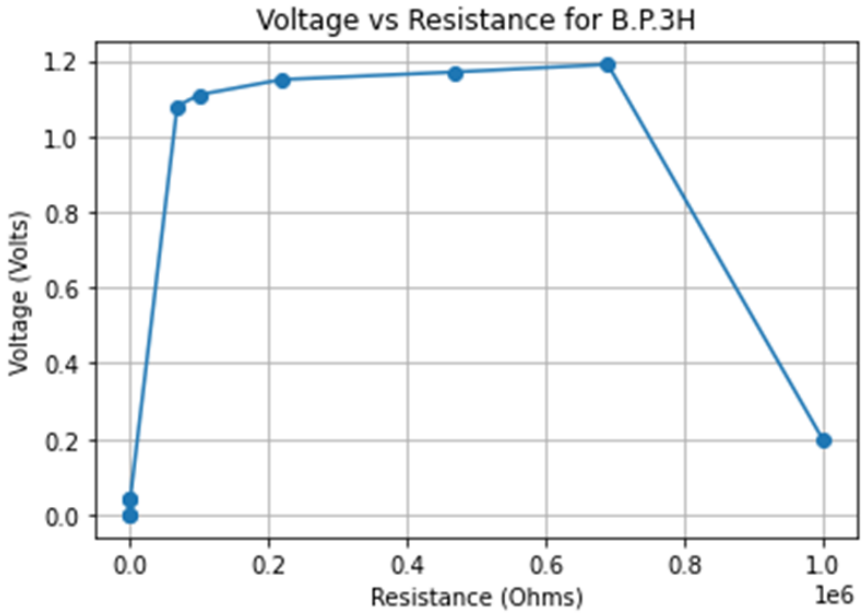

Figure 27: Data set plot for the B.P.3H cell showing voltage values observed at differing resistance values.

Table 8: Control Voltage Values for Resistance Tests

Cell Tested	Control									
Resistance	1 Ω	11 Ω	100 Ω	105 Ω	68 KΩ	100 KΩ	219 KΩ	470 KΩ	690 KΩ	1 MΩ
Voltage	0.00V	0.00V	0.01V	0.02V	1.14V	1.17V	1.20V	1.22V	1.23V	0.18V

Table 8: Shows the voltage values found for each subsequent test of varied resistance observed after the cells sat for 110-days for the Control cell.

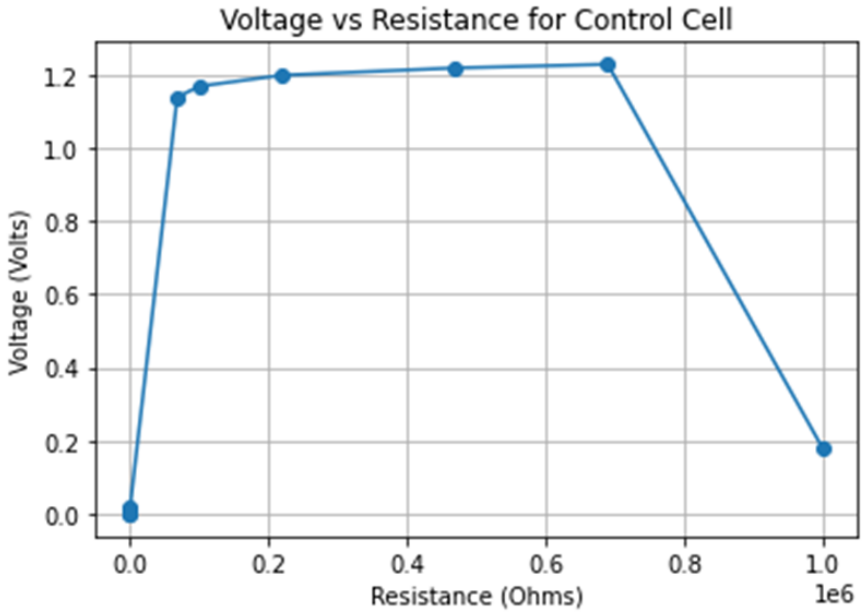

Figure 28: Data set plot for the Control cell showing voltage values observed at differing resistance values.

Table 9: B. $FeSO_4$ Voltage Values for Resistance Tests

Cell Tested	B. $FeSO_4$									
Resistance	1 Ω	11 Ω	100 Ω	105 Ω	68 KΩ	100 KΩ	219 KΩ	470 KΩ	690 KΩ	1 MΩ
Voltage	0.01V	0.01V	0.03V	0.04V	1.16V	1.20V	1.23V	1.25V	1.26V	0.18V

Table 9: Shows the voltage values found for each subsequent test of varied resistance observed after the cells sat for 110 days for the $B.FeSO_4$ cell.

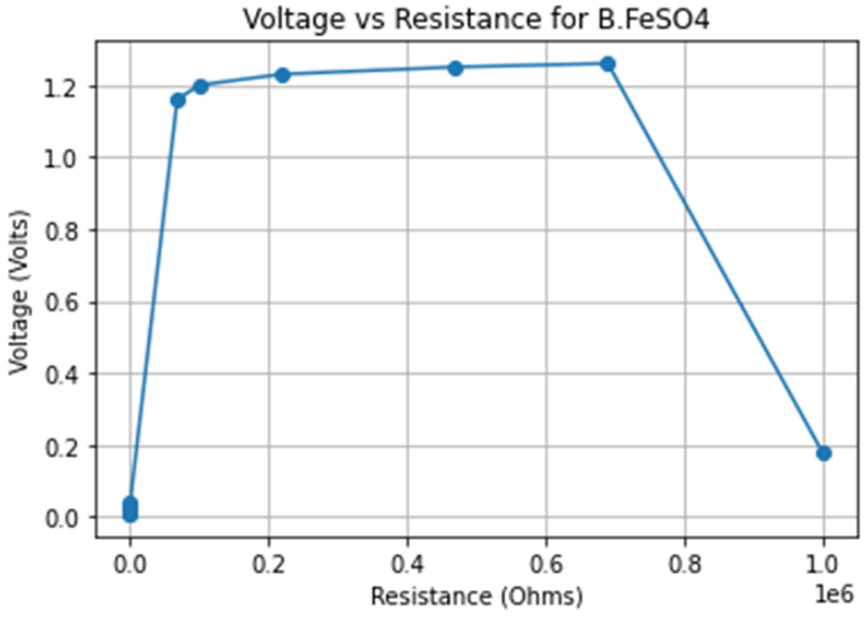

Figure 29: Data set plot for the $B.FeSO_4$ cell showing voltage values observed at differing resistance values.

.

Table 10: B. $KNaC_4H_4O_6$ Voltage Values for Resistance Tests

Cell Tested	B. $KNaC_4H_4O_6$									
Resistance	1 Ω	11 Ω	100 Ω	105 Ω	68 KΩ	100 KΩ	219 KΩ	470 KΩ	690 KΩ	1 MΩ
Voltage	0.01V	0.01V	0.01V	0.01V	0.90V	0.95V	1.01V	1.04V	1.03V	0.06V

Table 10: Shows the voltage values found for each subsequent test of varied resistance observed after the cells sat for 110-days for the $B.KNaC_4H_4O_6$ cell.

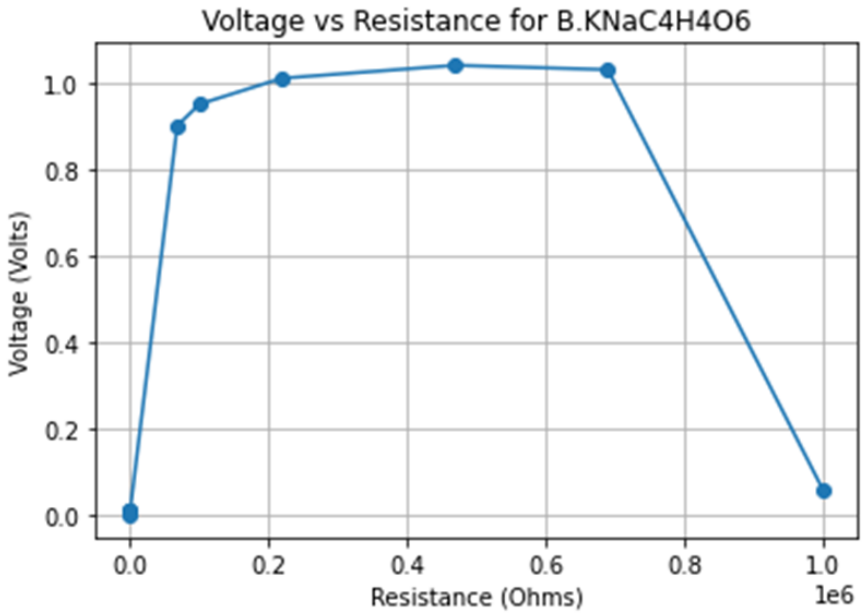

Figure 30: Data set plot for the $B.KNaC_4H_4O_6$ cell showing voltage values observed at differing resistance values.

Table 11: B.NaCO Voltage Values for Resistance Tests

Cell Tested	B. NaCO									
Resistance	1 Ω	11 Ω	100 Ω	105 Ω	68 KΩ	100 KΩ	219 KΩ	470 KΩ	690 KΩ	1 MΩ
Voltage	0.01V	0.01V	0.14V	0.14V	1.20V	1.20V	1.21V	1.23V	1.24V	0.58V

Table 11: Shows the voltage values found for each subsequent test of varied resistance observed after the cells sat for 110-days for the B. NaCO cell.

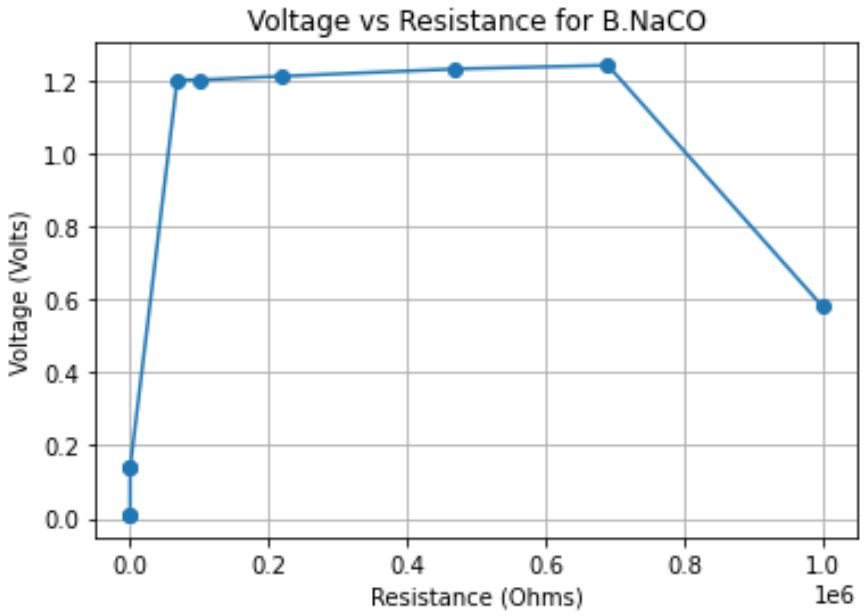

Figure 31: Data set plot for the B. NaCO cell showing voltage values observed at differing resistance values.

Following the completion of the resistance tests, the batteries were carefully returned to airtight plastic bags and allowed to undergo a voltage 'bounce back' process. Whereby a specific duration of 15-minutes was then allocated for the voltage restoration. After the 15-minute period had elapsed the voltage for each cell was assessed solely by observing the cathode and anode terminals using a digital multimeter and its respective probes. It's important to note that since the varied resistor test was conducted after the 110-day time period had elapsed, the voltage measured after the 15-minute interval was compared to the maximum observed voltage prior to the varied resistance test. The resulting values were tabulated in Table 12, and their corresponding graphical representation is depicted in the subsequent Figure 32. Overall, the outcomes of this observation aligned with predictive expectations, with one notable exception observed in the S.A.2H cell. Surprisingly, the voltage measured after allowing the cells to rest for 15-minutes was found to exceed the initial voltage for the S.A.2H cell and hence, deviating from anticipated trends observed by the other solid-state cells tested in this manner.

Table 12: Voltage Values 15-Minutes After Resistance Tests

Cell Tested	S.A.2H	B.A.2H	B.P.1H	B.P.2H	B.P.3H	Control	B. $FeSO_4$	B. $KNaC_4H_4O_6$	B. NaCO
Voltage Observed Prior to Resistance Testing	1.19V	0.86V	1.20V	1.25V	1.24V	1.26V	1.32V	1.15V	1.33V
Voltage Observed After 15min had Elapsed	1.27V	0.82V	1.19V	1.18V	1.20V	1.22V	1.28V	1.10V	1.32V

Table 12: Shows the voltage values observed after the cells sat for 110-days compared to the voltage values that were tabulated 15 minutes after the varied voltage tests.

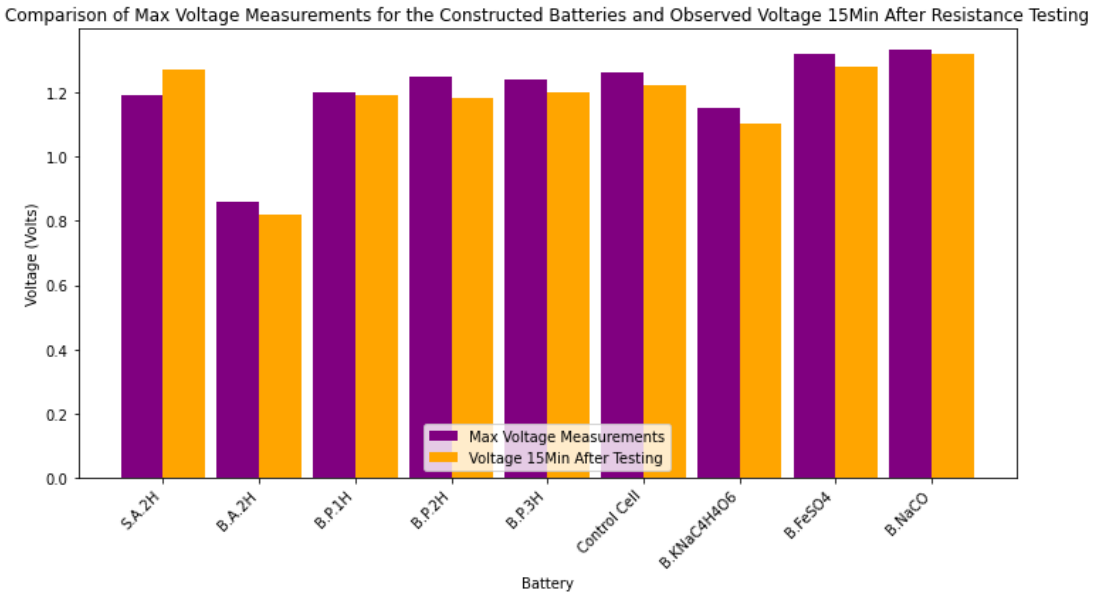

Figure 32: The voltage comparison for the initial voltage values of the cells after the 110-day isolation and the voltage values found after isolation of the cells following the varied resistance test, shown in purple and orange respectively.

Once the cells were observed to regain their full cell voltage, they were deliberately subjected to a short circuit until the measured voltage for each cell reached 0 V. Upon reaching this state, the short circuit was promptly removed, and detailed measurements were taken to determine the time required for each cell to 'bounce back' to specific percentage values relative to the full cell voltage. These detailed results, which can be observed in the subsequent data sets, exhibit a wide range when analyzing the time taken to achieve 95% of the initial voltage parameter. In response to this variability, an additional graph has been provided, wherein the measured time values are depicted more clearly by excluding results exceeding 40 seconds. However, it's important to note that the tabulated data in Table 13, is solely comprised of the actual values obtained during the execution of this test, providing a comprehensive record of the observed outcomes.

Table 13: Time Needed for Voltage to be Regained

Cell Tested	S.A.2H	B.A.2H	B.P.1H	B.P.2H	B.P.3H	Control	B. $FeSO_4$	B. $KNaC_4H_4O_6$	B. NaCO
Voltage Observed Prior to Short Circuit	1.33V	1.20V	1.28V	1.28V	1.29V	1.26V	1.32V	1.17V	1.36V
Time Elapsed to Reach 50% of Initial Voltage	<1s	<1s	<1s	<1s	<1s	<1s	<1s	<1s	<1s
Time Elapsed to Reach 80% of Initial Voltage	<1s	<1s	<1s	2s	1s	1s	<1s	<1s	<1s
Time Elapsed to Reach 90% of Initial Voltage	6s	4s	1s	27s	2s	3s	<1s	<1s	1s
Time Elapsed to Reach 95% of Initial Voltage	7s	9s	9s	260s	28s	15s	1s	1s	3s

Table 13: Shows the voltage values observed after multiple tests have been conducted on the cells and the time observed to reach specific percentage values of these voltages. Note all initial voltage values for the exception of the Control cell have actually been observed to show an increase in resting full cell voltage.

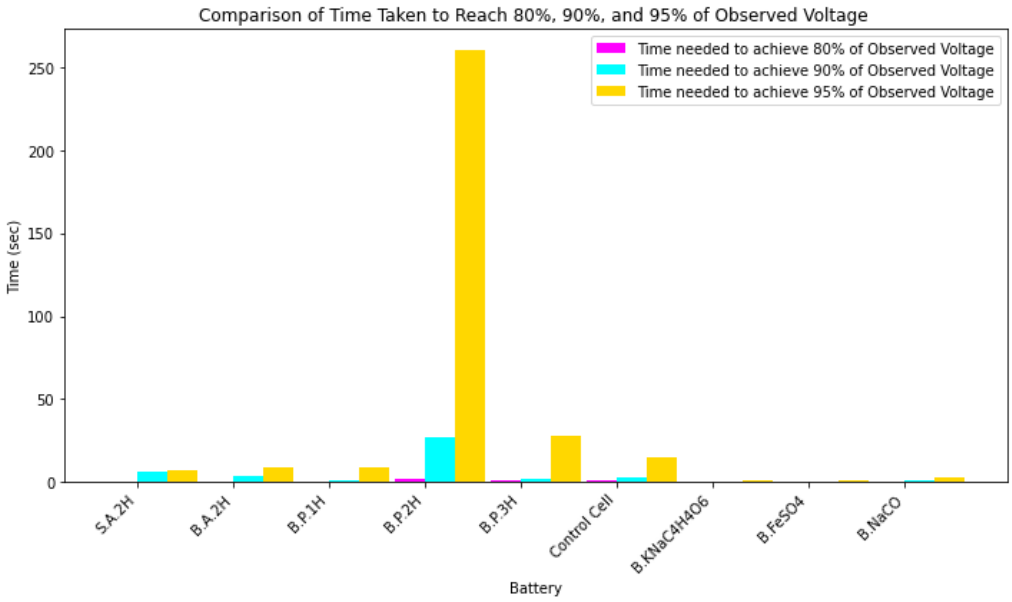

Figure 33: Shows the unaltered data set from the timed results for the cells to achieve specific percentages of the initial full cell voltage. Note the 50% parameter has been disregarded due to the time needed for all cells being found to be less than 1 second.

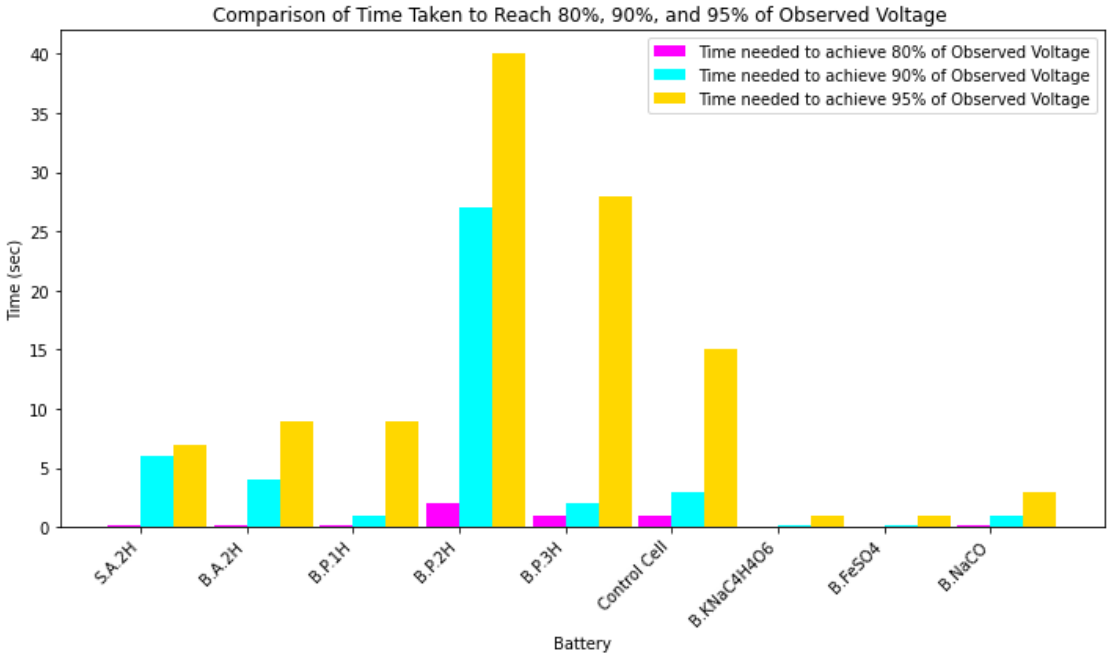

Figure 34: Shows the altered data set from the timed results for the cells to achieve specific percentages of the initial full cell voltage, where the observed time after 40 seconds has been disregarded. Note the 50% parameter has also been disregarded in this graph due to the time needed for all cells being found to be less than 1 second.

B. Current Measurements Through Circuits

The dataset presented in Table 14 is comprised of the short circuit current values obtained on the day the cells were constructed, representing the highest recorded values throughout the experiment. Markedly, it is of significance that both the Control cell and the S.A.2H cell yielded identical and simultaneously the highest short circuit current values among all tested cells at this time. Furthermore, aside from the Control and S.A.2H cells, the B. $FeSO_4$ and B.NaCO cells were observed to yield the minimum and maximum currents, respectively.

Table 14: Initial Short Circuit Current Values

Cell Tested	S.A.2H	B.A.2H	B.P.1H	B.P.2H	B.P.3H	Control	B. $FeSO_4$	B. $KNaC_4H_4O_6$	B.NaCO
Short Cir. Currents	98mA	31mA	35mA	32mA	33mA	98mA	22mA	29mA	41mA

Table 14: Shows the short circuit current values. Note that these current values observed here should be the largest observed throughout the experiment.

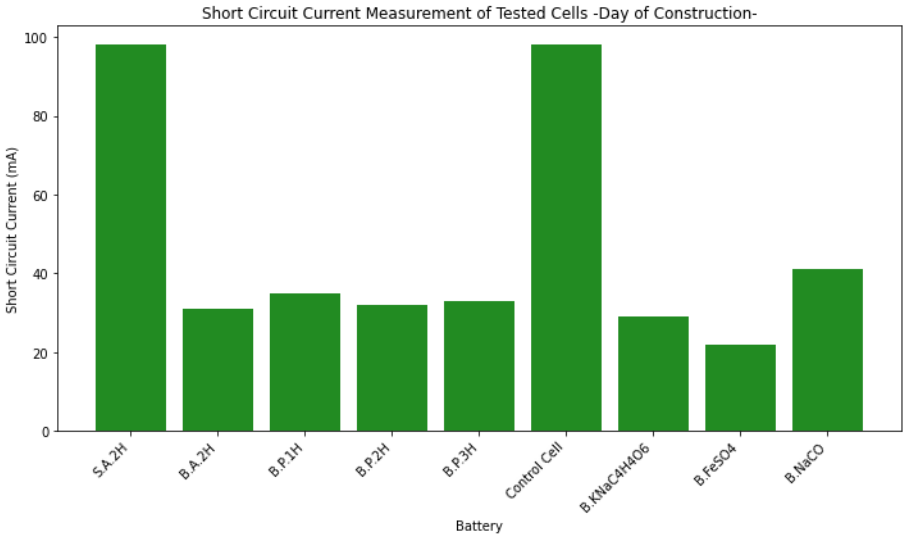

Figure 35: Shows the short circuit currents found for each cell on the day of construction. Note aside from two of the values it is clear to see that these values are relatively close to one another.

Below in Table 15, the dataset depicts the short circuit current values obtained following the 110-day isolation period observed by the cells. This tabulated information serves to highlight a significant challenge encountered by these types of cells. Upon examination of these new values, it became apparent that all cells were no longer capable of generating the same level of current that was previously observed. In fact, the observed current generation had decreased by two orders of magnitude. However, amidst the collection of these data points, intriguing behaviors were detected in both the B. $FeSO_4$ cell and the B.NaCO cell. These unexpected behaviors, while not immediately evident from the provided information, will be thoroughly explored and discussed in detail in the conclusion section.

Table 15: Short Circuit Current Values After 110-Days

Cell Tested	S.A.2H	B.A.2H	B.P.1H	B.P.2H	B.P.3H	Control	B. $FeSO_4$	B. $KNaC_4H_4O_6$	B.NaCO
Short Cir. Currents	0.26mA	0.56mA	0.86mA	0.95mA	0.43mA	0.45mA	0.50mA	0.17mA	1.62mA

Table 15: Shows the short circuit current values after allowing the cells to be placed in isolation for 110-days.

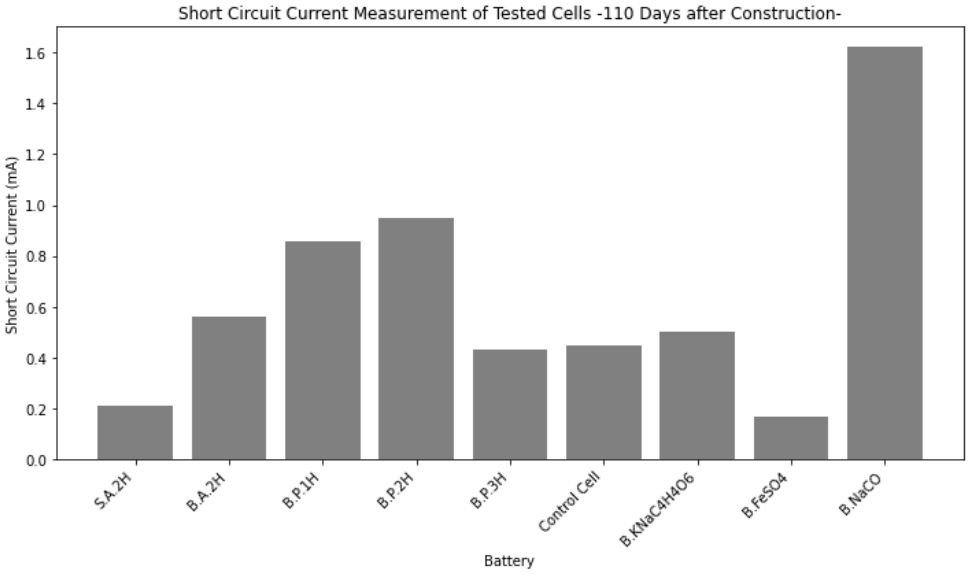

Figure 36: Shows the short circuit currents found for each cell 110-days after construction.

The graphical representation in Figure 37 vividly illustrates a significant shift in short circuit currents observed, made evident by a comparative analysis of the tabulated data sourced from both Table 14 and Table 15. While Figure 36 above provides a clear indication that the B.NaCO cell outperforms its counterparts, a closer examination

reveals that even this current generation does not match the levels attained by previous iterations of cell currents. This nuanced and comparative perspective of current generation across different cell configurations aids to analyze if any of these solid-state cells can retain being competitive in the energy market.

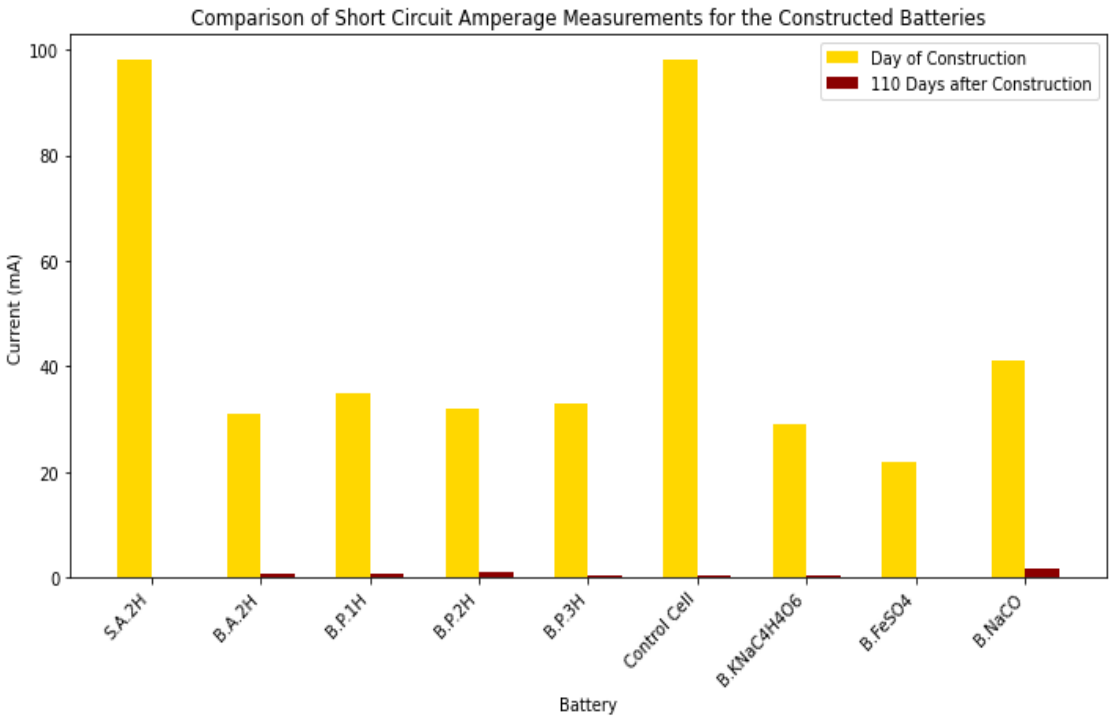

Figure 37: This is a graphical comparison of the tabulated data from both Table 14 and Table 15 showing short circuit comparison between the two time periods.

The subsequent measurements analyzed pertain to running amperage values, which were derived from the maximum steady-state voltages documented in Tables 3 through 11.

To obtain these values, each cell was systematically subjected to different levels of resistance within a circuit. This involved conducting tests with varying resistances, including 68 KΩ, 100 KΩ, and 219 KΩ. The ensuing set of data is comprised of both tabulated and graphical plotted representations illustrating the observed amperage corresponding to the specified load resistances that were tested. This comprehensive analysis provides insights into the dynamic interplay between voltage, resistance, and amperage across the range of conditions for the crystal cells that were tested.

Table 16: Current Values After 110-Days in Running Loads

Cell Tested	S.A.2H	B.A.2H	B.P.1H	B.P.2H	B.P.3H	Control	B. $FeSO_4$	B. $KNaC_4H_4O_6$	B. NaCO
Amperage Observed with a Load Resistance of 68KΩ	18.2μA	18.4μA	18.4μA	17.7μA	18.4μA	18.3μA	18.4μA	14.6μA	19.9μA
Amperage Observed with a Load Resistance of 100KΩ	12.3μA	12.1μA	12.3μA	11.9μA	12.4μA	12.3μA	12.6μA	10.0μA	13.3μA
Amperage Observed with a Load Resistance of 219KΩ	5.8μA	5.6μA	5.7μA	5.5μA	5.8μA	5.7μA	5.9μA	4.8μA	5.9μA

Table 16: Shows the running current values observed by the cells that sat for 110-days and placed under the denoted amounts of resistance listed in the table.

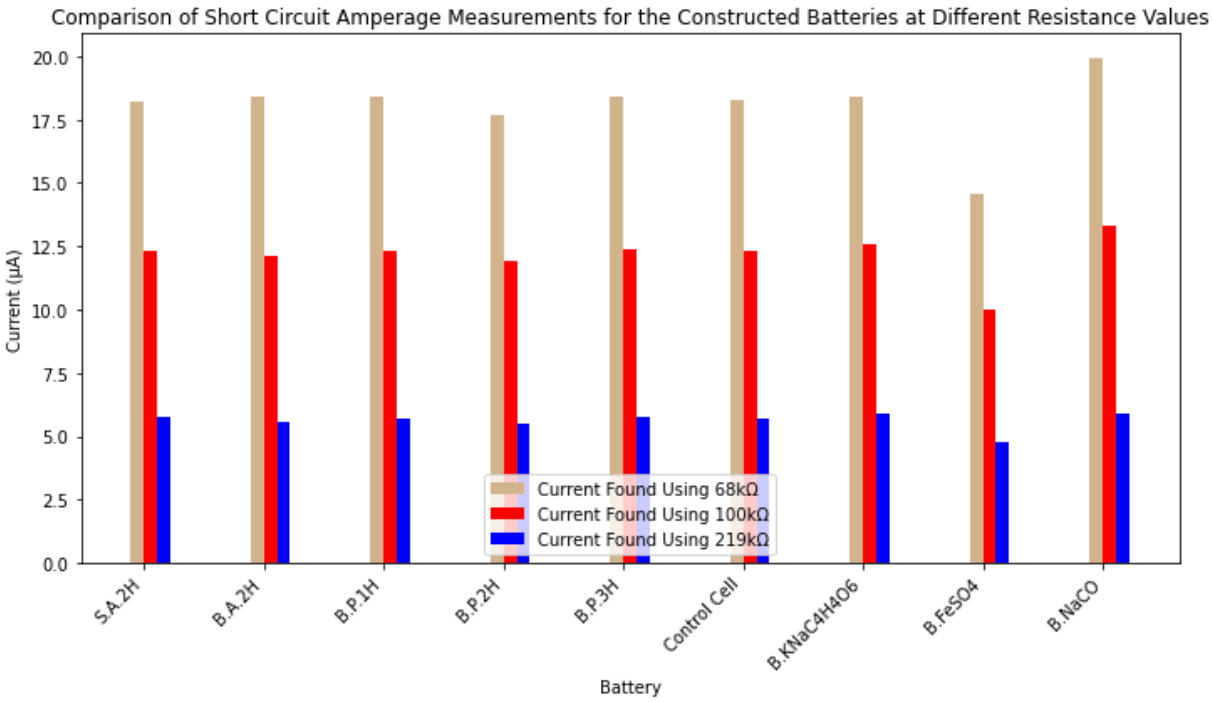

Figure 38: This is a comparison of the tabulated data from Table 16 showing the running current amperages at differing resistances. Note that the B.NaCO cell has the largest range of running current at these given load resistances.

C. Mass Values and Statistical Analysis

The subsequent charts provide a comprehensive overview of the total mass for each constructed cell, illuminating how the mass ratio percentage can be interpreted for individual cell. The mass analysis is intricately subdivided into four key categories, each shedding light on distinct aspects of the cell construction process; the cathode which is inclusive of any housing components, both the larger and smaller diameter anodes specific to each listed cell, the cooled and solid resultant mass of the crystal substrate that was observed to form within the cavity of each cell, and, for the cells that are applicable, the mass attributed to the dopant employed in the doping process. Notably, the dopant that was incorporated into the substrate mixture prior to the heating process, was closely observed and thus maintained a consistent 2% ratio relative to the total mass from which the crystal substrate was derived. This systematic and meticulous approach was taken to comprehensively analyze the mass composition of each cell and its constituent elements.

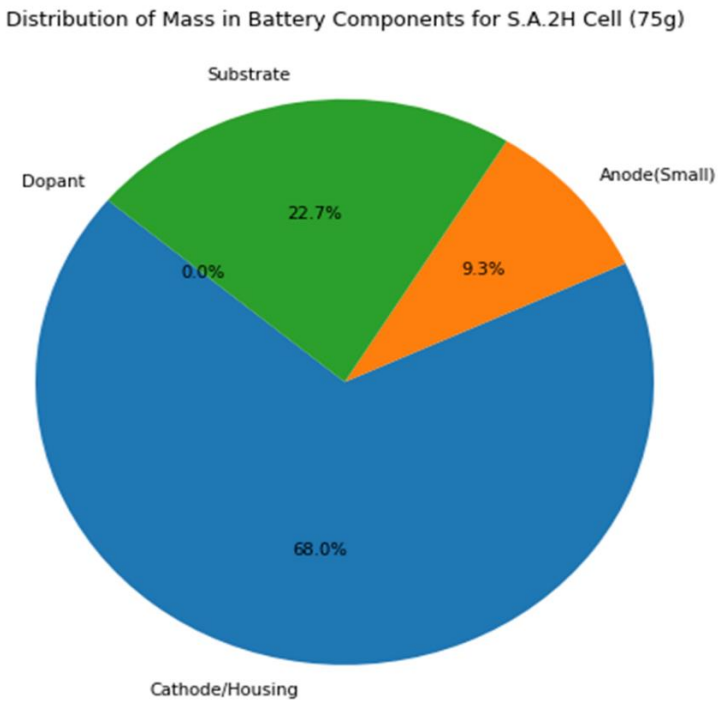

Figure 39: Chart showing how the mass breaks down for each major component in the S.A.2H cell.

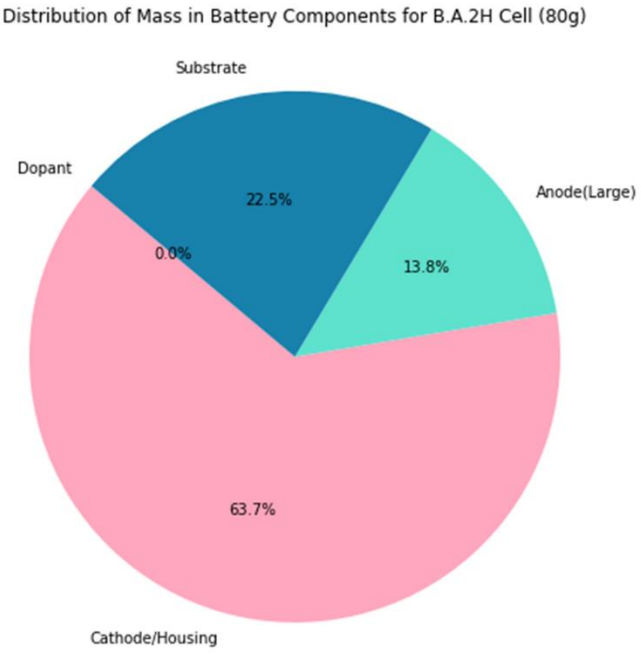

Figure 40: Chart showing how the mass breaks down for each major component in the B.A.2H cell.

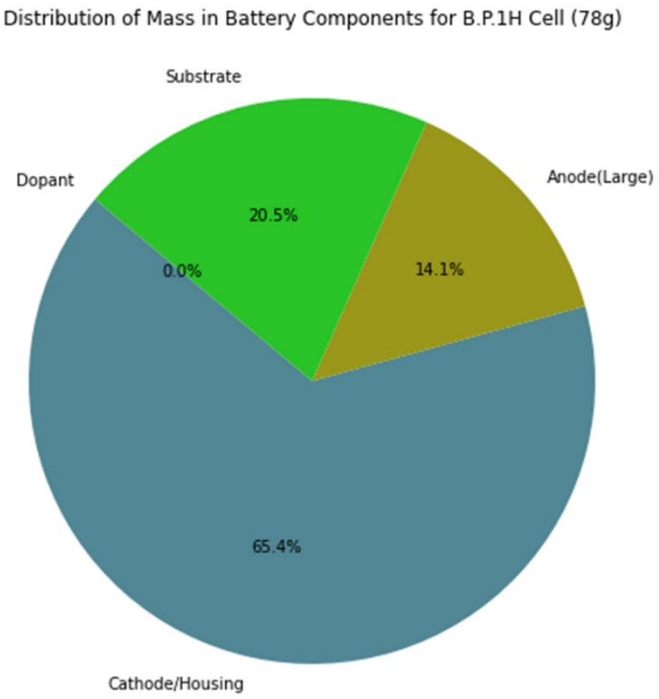

Figure 41: Chart showing how the mass breaks down for each major component in the B.P.1H cell.

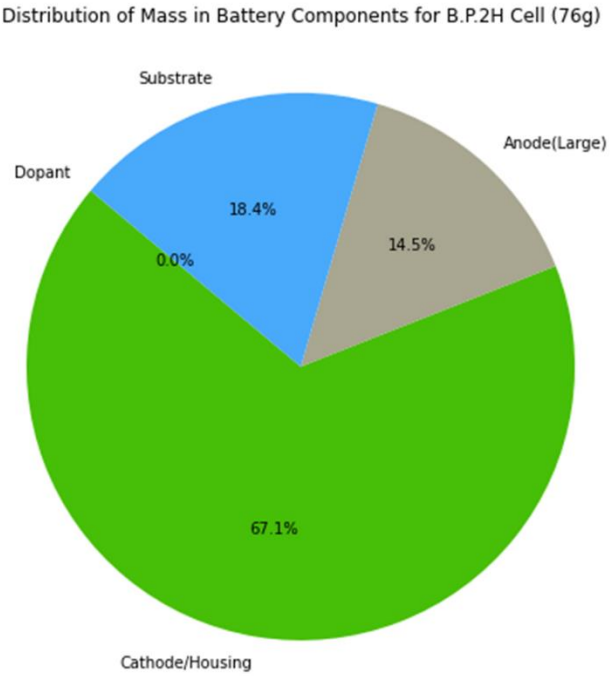

Figure 42: Chart showing how the mass breaks down for each major component in the B.P.2H cell.

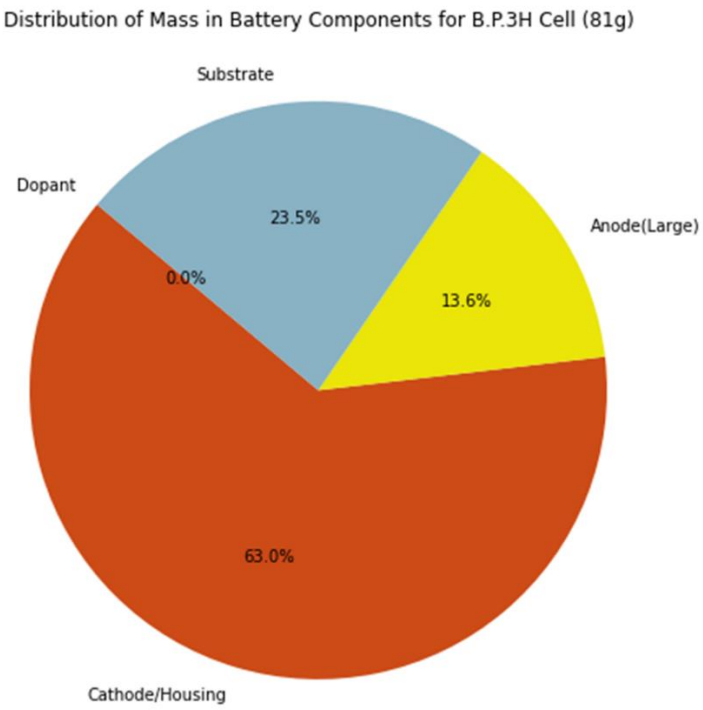

Figure 43: Chart showing how the mass breaks down for each major component in the B.P.3H cell.

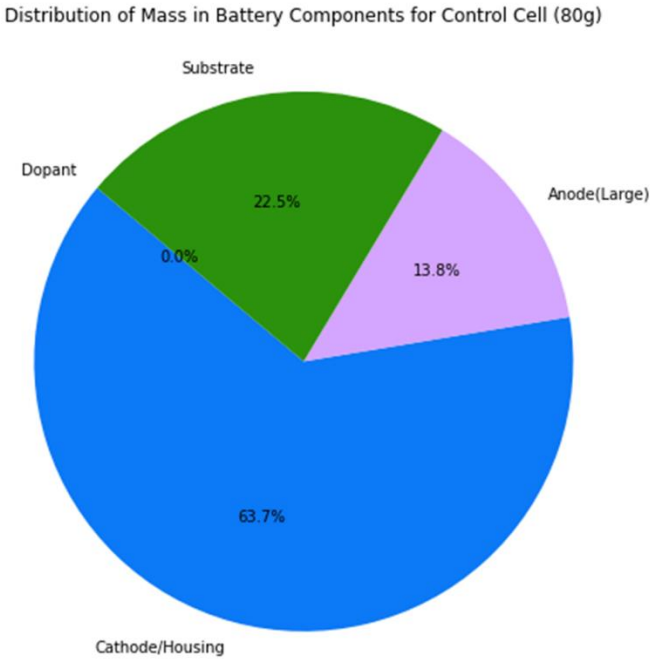

Figure 44: Chart showing how the mass breaks down for each major component in the Control cell.

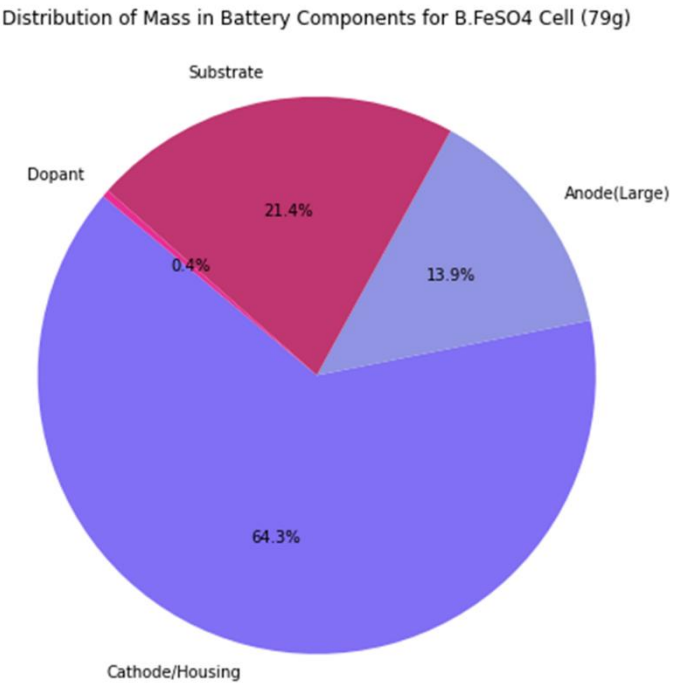

Figure 45: Chart showing how the mass breaks down for each major component in the $B.FeSO_4$ cell.

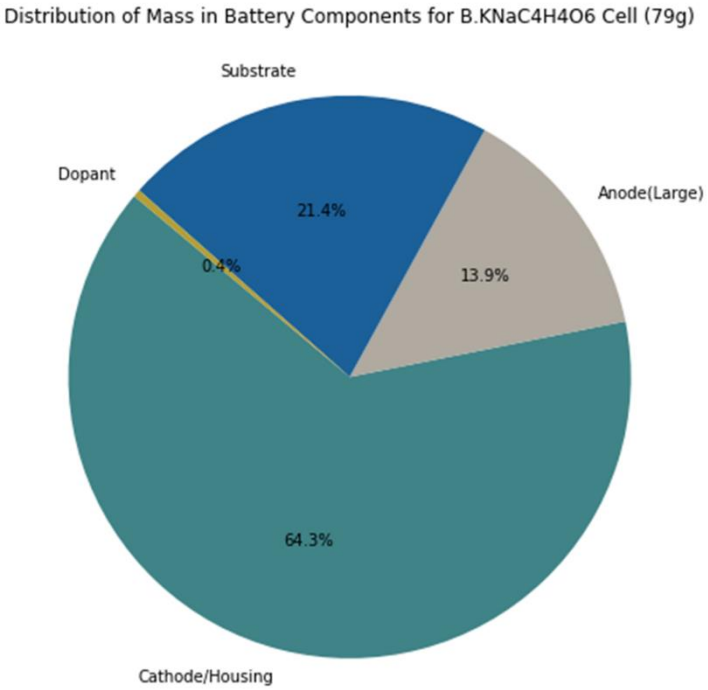

Figure 46: Chart showing how the mass breaks down for each major component in the $B.KNaC_4H_4O_6$ cell.

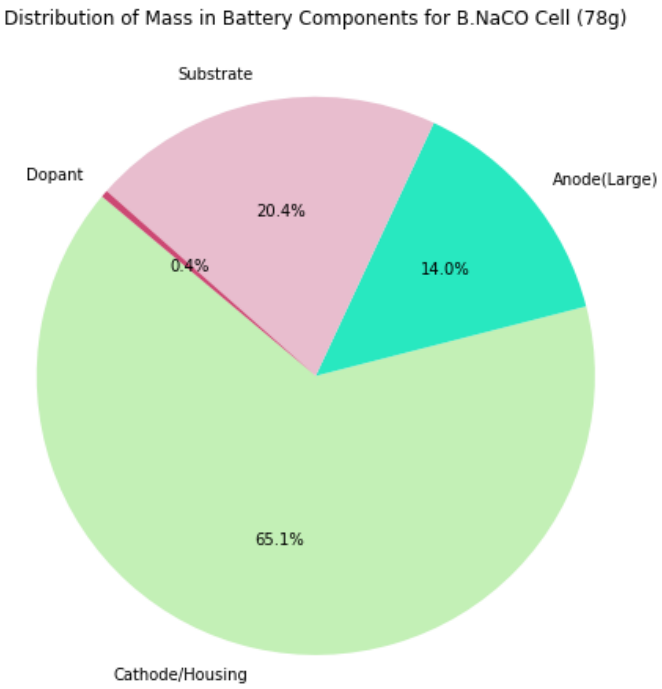

Figure 47: Chart showing how the mass breaks down for each major component in the B.NaCO cell.

Following the presentation of tabulated masses in Table 17 and the subsequent depiction in Figure 48, it is important to note that the primary focus is not solely on the comparison of masses between cells. Instead, the emphasis lies in the rationale behind maintaining as much uniformity in the results as possible. Admittedly, achieving robust statistical significance with such a small data set, comprising only nine cells, presents obvious challenges. However, these results are included in good faith, with the hope of discerning any observed mass differences through statistical analysis. Notably, statistical analyses were conducted for all nine cells collectively, rather than subdividing them into smaller categories based on cell types, owing to the limited sample size. Consequently,

total mass emerged as the sole mass value considered, accentuating the meticulous approach taken to ensure methodological rigor despite inherent limitations in sample size.

Table 17: Constructed Cell Mass Values

Cell Tested	S.A.2H	B.A.2H	B.P.1H	B.P.2H	B.P.3H	Control	B. $FeSO_4$	B. $KNaC_4H_4O_6$	B.NaCO
Total Mass of Cell	75g	80g	78g	76g	81g	80g	79g	79g	78g

Table 17: Shows the total mass values for the constructed cells.

Regarding the masses of the cells, it's noteworthy that the cathode portions were uniformly constructed to weigh 51 grams each. In contrast, the anodes varied in diameter, with the larger diameter anodes weighing 11 grams and the smaller diameter anodes weighing 7 grams. Consequently, the variation in mass primarily pertained to the crystal cell component of the cells, ensuring that any discrepancies in total mass closely mirrored potential differences in electrical properties. This meticulous control over mass variations emphasizes the importance of accurately assessing the impact of different mass configurations on the electrical characteristics of the cells tested.

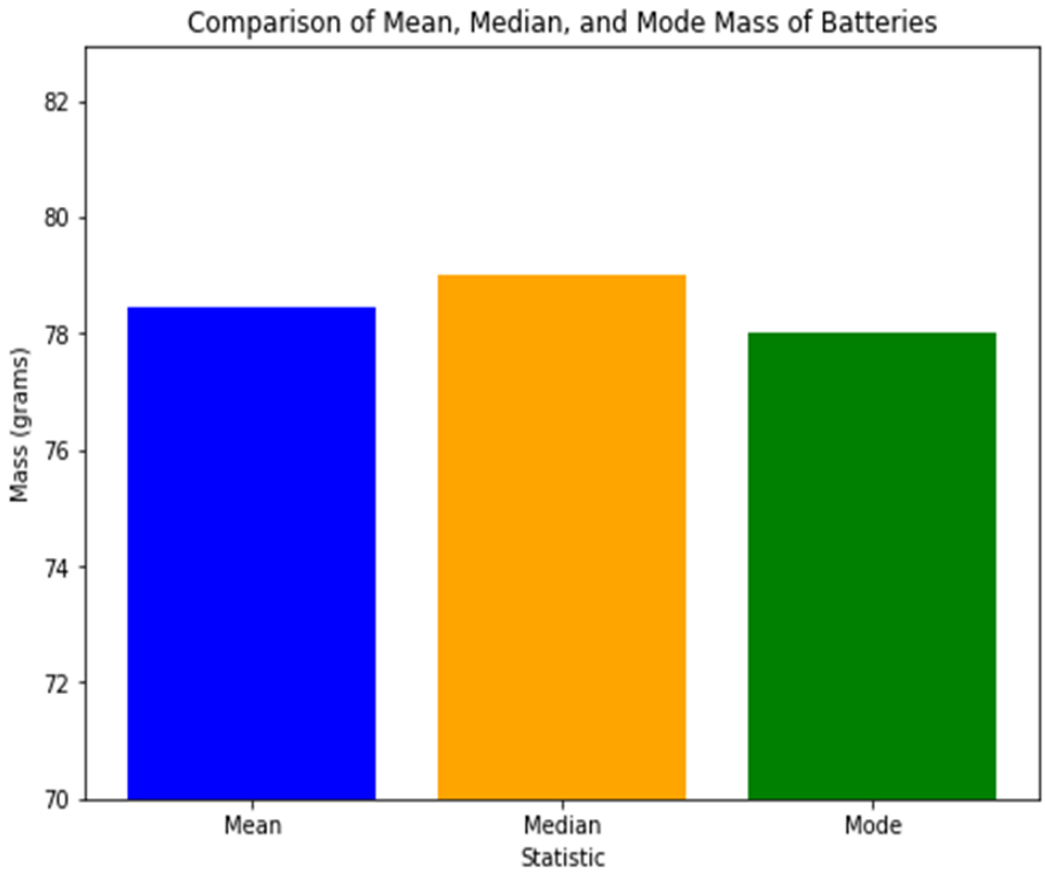

Figure 48: Shows the mass values for the constructed cells being analyzed using the statistical methods of mean, median, and mode.

Density and molar mass are fundamental properties intricately linked to the measured mass values of a substance. However, it's important to clarify that the dataset presented here does not stem from the experimental procedures but rather reflects the inherent characteristics of the dopants employed in the three doped cells. The tabulated data serves not only as a reference point for this specific dataset but also lays the groundwork for evaluating any future dopants utilized in subsequent research endeavors.

Table 18: Mass Properties for Dopants Used

Cell Tested	B. $FeSO_4$	B. $KNaC_4H_4O_6$	B.NaCO
Molar Mass of Dopant	151.91 $\frac{g}{mol}$	105.99 $\frac{g}{mol}$	282.22 $\frac{g}{mol}$
Density of Dopant	1.79 $\frac{g}{cm^3}$	2.84 $\frac{g}{cm^3}$	2.54 $\frac{g}{cm^3}$

Table 18: Shows the known molar mass and density values for the constructed cells that were doped.

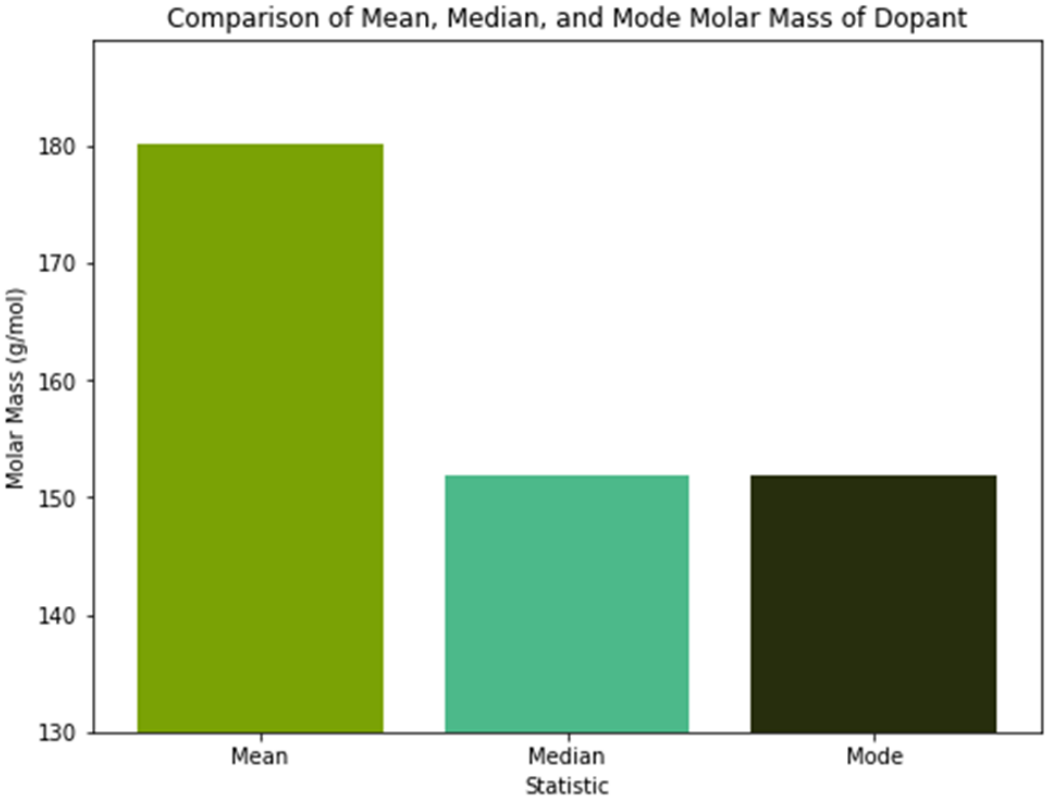

Figure 49: Shows how the known molar mass between the three dopants used when analyzed using the values and finding the mean, median, and mode.

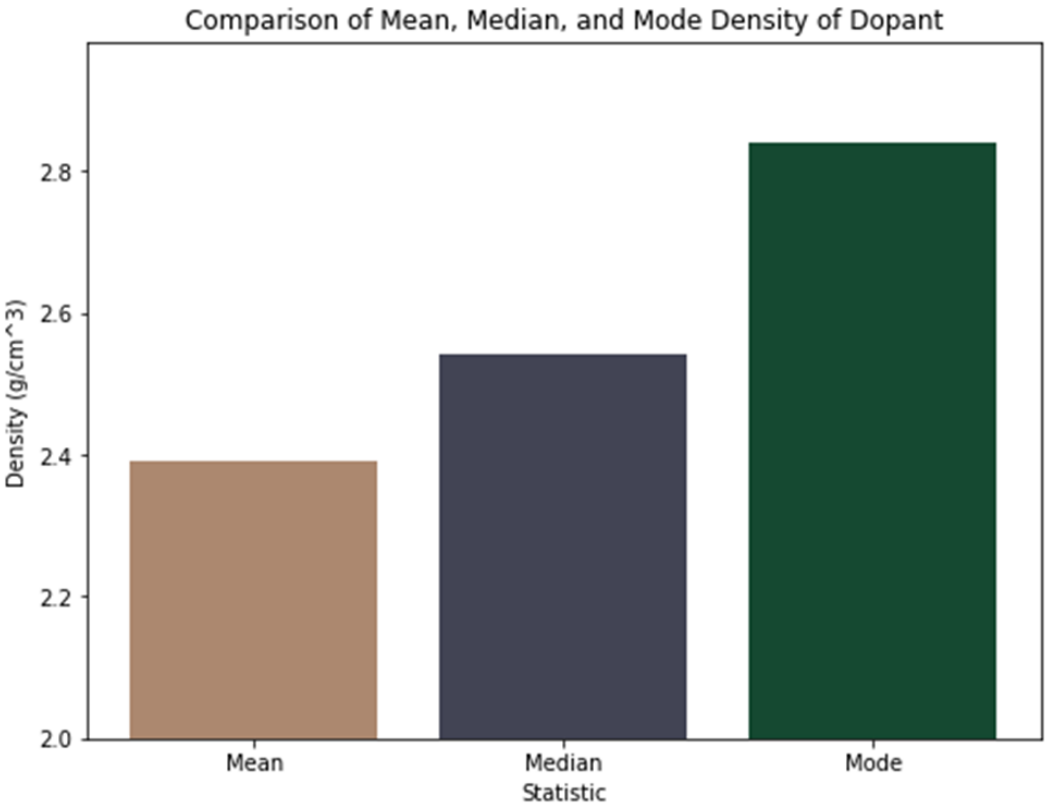

Figure 50: Shows how the known density between the three dopants used when analyzed using the values and finding the mean, median, and mode.

V. Discussion and Conclusions

Throughout the testing phase of this project, a plethora of unexpected outcomes unfolded. Initially, the S.A.2H cell emerged as the frontrunner in terms of voltage potential, despite featuring a smaller diameter anode. This observation raised intriguing questions regarding the underlying mechanisms. One plausible explanation could be attributed to the increased volume available for the crystal substrate within this particular cell. However, it is noteworthy that this cell exhibited the smallest mass among those tested. Consequently, it is conceivable that it failed to completely occupy the cavity with solid crystal material following the cooling process. This discrepancy prompts speculation regarding the electrochemical processes initiated within the cell. It is conceivable that the utilization of oxyacetylene as the heating source during fabrication may have induced more vigorous effervescence reactions, potentially hindering the complete filling of the cavity during the cooling phase. Further investigation is warranted to elucidate the intricate interplay between fabrication methods, electrode dimensions, and resulting electrochemical behavior in solid-state crystal cell batteries.

Furthermore, the findings pertaining to the various aspects of annealed cells yielded a diverse array of outcomes. Within this domain of investigation, one particular subset stood out prominently, namely, the data set for the B.P.2H cell. Notably, this cell exhibited a distinct characteristic in terms of the time required for voltage recovery, commonly referred to as 'bounce back', a stable trait in batteries of this nature. While the majority of tested cells displayed a 'bounce back' voltage recovery within tens of seconds, the B.P.2H cell demonstrated a considerably prolonged recovery period, spanning multiple minutes,

following placement in a short circuit. Adding complexity to these perplexing results was the observation that the other two cells annealed using the propane method did not manifest this extended recharging duration. Intriguingly, the cell under scrutiny for this phenomenon underwent the annealing process twice, whereas the remaining two cells that were also subjected to the propane heating method, namely B.P.1H and B.P.3H, underwent the annealing process once and three times, respectively. These findings underscore the complexity of the annealing process and its nuanced impact on battery performance. Consequently, it is evident that further exploration and experimentation in annealing the cathodes of solid-state crystal cell batteries are warranted to unravel the underlying mechanisms governing their electrochemical behavior comprehensively.

Despite initial observations indicating a decline in voltage values shortly after construction, a notable anomaly emerged within the dataset. Specifically, the $B.FeSO_4$ cell not only exhibited greater stability in maintaining cell potential but also demonstrated an unexpected increase in voltage over time. This intriguing phenomenon underscores the complexity of doping effects on battery performance. Moreover, the unexpected outcomes were not confined to the $B.FeSO_4$ cell alone. Another instance of unexpected behavior was observed in the B.NaCO doped crystal cell. Following an isolation period of 110-days, both cells were subjected to a short current. Contrary to expectations, after the anticipated initial current drop, both cells exhibited a gradual increase in amperage output. This intriguing observation suggests a potential adaptive mechanism wherein the cells endeavor to overcome induced short circuits by augmenting their power generation capacity. These findings highlight the need for further in-depth

investigation and research, adopting a more focused and systematic approach. Additionally, expanding the dataset through continued experimentation is essential to discern genuine trends from potentially spurious outliers.

The potential of crystal cell batteries to serve as a linchpin in addressing the myriad energy challenges currently hampering societal progress is profound. The impetus driving the exploration of improved battery technologies is multifaceted, spurred by a confluence of factors encompassing the modern worlds escalating energy storage demands, ever growing environmental imperatives, safety considerations, and the imperative to curtail costs. The trajectory of further research in this domain holds considerable sway over contemporary perceptions and approaches to meeting energy needs for the people encompassed in an energy demanding society.

In the relentless march toward a modern, technologically savvy era, many analysts contend that energy production and storage represent paramount concerns for every nation. With the burgeoning demand for portable electronic devices, electric vehicles, renewable energy sources, and an increasingly burdened electrical grid, the imperative for higher-capacity and more efficient batteries is becoming ever more pressing. Consequently, it stands to reason that advancements in battery technology, such as solid-state crystal cells, could serve as a key player in enhancing our modern way of life and, potentially, mitigating environmental degradation.

Solid-state crystal cell batteries could emerge as a promising solution for energy storage, offering the capability to store and provide power for substantially longer durations compared to conventional batteries. Moreover, their scalability renders them viable for providing large electrical potentials, catering to individual modern homes or remote structures distant from urban amenities. Importantly, these cells boast environmental advantages over conventional batteries, as they are constructed using metals and compounds abundant on our planet. Not only are these raw materials readily available, but their extraction processes can also be conducted with greater emphasis on environmental preservation compared to current lithium mining practices.

Environmental conservation is further bolstered by the reduction of greenhouse gas emissions and manufacturing practices associated with crystal cell batteries, contrasting starkly with the environmental concerns tied to traditional lithium-ion batteries. Ensuring consumer safety is another pivotal driver for battery research, given the well-documented risks of lithium-ion battery rupture and fire hazards. New battery technologies, such as crystal cell batteries, hold the promise of mitigating such safety risks while potentially reducing the cost of energy storage. This multi-faceted approach to addressing energy challenges underscores the transformative potential of crystal cell batteries and underscores the urgent need for continued research and development in this field.

VI. REFERENCES

Admin. (2023, August 16). *Semiconductors - types, examples, properties, application and uses*. BYJUS. https://byjus.com/jee/semiconductors/

Blanc, L. (2020, November 3). *Developing nano-sized cathode materials for magnesium ion batteries | Lauren Blanc*. YouTube. https://www.youtube.com/watch?v=GH5rC4MiTtA

Connor, N. (2023, July 24). *Copper (II) oxide: Formula, properties & application*. Material Properties. https://material-properties.org/copper-ii-oxide/

Cuo crystal structure. SpringerMaterials. (n.d.). https://materials.springer.com/isp/crystallographic/docs/sd_0542121

Faizan, A. (2024, April 3). *Ammeter- definition and working principle*. Electrical Academia. https://electricalacademia.com/instrumentation-and-measurements/ammeter-definition-and-working-principle/

If a cell ,cell reaction is mg+cu2+aq= CU +mg2+aq. if Mg and Cu e Red _2.37V and+0.34 than cell emf is?. byju. (n.d.). https://byjus.com/question-answer/if-a-cell-cell-reaction-is-mg-cu2-aq-cu-mg2-aq-if-mg-and/

Lasersaber. (2015, October 30). *Crystal cells have been going for 4+ years! - crystal cells duration testing update*. YouTube. https://www.youtube.com/watch?v=3cJFkIDImuM

logos2012. (2016, September 22). *Ethyl mercaptan chemical structure vector image on VectorStock*. VectorStock.

https://www.vectorstock.com/royalty-free-vector/ethyl-mercaptan-chemical-structure-vector-10742743

Rudolph, G., & Hooge, C. (n.d.). *20.2 Ohm's law: Resistance and simple circuits*. BCIT Physics 0312 Textbook. https://pressbooks.bccampus.ca/physics0312chooge/chapter/20-2-ohms-law-resistance-and-simple-circuits/